Neurobiology of Disease 204 (2025) 106769

Contents lists available at ScienceDirect

Neurobiology of Disease

journal homepage: www.elsevier.com/locate/ynbdi

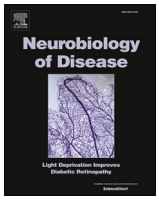

Instationary metabolic flux analysis reveals that NPC1 inhibition increases glycolysis and decreases mitochondrial metabolism in brain microvascular endothelial cells

Bilal Moiz [a], Matthew Walls [a], Viviana Alpizar Vargas [a], Anirudh Addepalli [a], Callie Weber [a], Andrew Li [a], Ganesh Sriram [b], Alisa Morss Clyne [a,*]

[a] Department of Bioengineering, University of Maryland, College Park, MD 20742, United States of America
[b] Department of Chemical and Biochemical Engineering, University of Maryland, College Park, MD 20742, United States of America

ARTICLE INFO

Keywords:
Niemann-pick disease type C
NPC1
Metabolism
Metabolic flux analysis
Systems biology
Glycolysis
Oxidative respiration
Endothelial cells
Blood-brain barrier

ABSTRACT

Niemann Pick Disease Type C (NP-C), a rare neurogenetic disease with no known cure, is caused by mutations in the cholesterol trafficking protein NPC1. Brain microvascular endothelial cells (BMEC) are thought to play a critical role in the pathogenesis of several neurodegenerative diseases; however, little is known about how these cells are altered in NP-C. In this study, we investigated how NPC1 inhibition perturbs BMEC metabolism in human induced pluripotent stem cell-derived BMEC (hiBMEC). We incorporated extracellular metabolite and isotope labeling data into an instationary metabolic flux analysis (INST-MFA) model to estimate intracellular metabolic fluxes. We found that NPC1 inhibition significantly increased glycolysis and pentose phosphate pathway flux while decreasing mitochondrial metabolism. These changes may have been driven by gene expression changes due to increased cholesterol biosynthesis, in addition to mitochondrial cholesterol accumulation. We corroborated these findings in primary BMEC, an alternative in vitro human brain endothelial model. Finally, we found that co-treatment with hydroxypropyl-β cyclodextrin (HPβCD) partially restored metabolic phenotype in U18666A-treated BMECs, suggesting that this drug may have therapeutic effects on the brain endothelium in NP-C. Together, our data highlight the importance of NPC1 in BMEC metabolism and implicate brain endothelial dysfunction in NP-C pathogenesis.

1. Introduction

Brain microvascular endothelial cells (BMEC), which line cerebral blood vessels and are an essential component of the blood-brain barrier (BBB), tightly regulate glucose entry into the brain. BMEC selectively take up glucose from the blood through apical glucose transporters. BMEC then either metabolize glucose for their own metabolic needs, or they transport the glucose into the brain through basolateral glucose transporters to fuel other brain cells (Yazdani et al., 2019). BMEC glucose transport is critical for neuronal health, as the brain primarily relies on glucose to fulfill its energetic requirements (Mergenthaler et al., 2013). Studies in rats suggest that ~95 % of glucose taken up by BMEC is available for transport to the brain parenchyma (Goldstein et al., 1977); however, brain glucose availability may be perturbed in pathological states which alter BMEC metabolic phenotype and cause BMECs to consume more glucose for their own needs, ultimately decreasing glucose availability for other brain cells.

Indeed, recent evidence implicates brain hypometabolism and BMEC dysfunction in neurological diseases, including amyotrophic lateral sclerosis, epilepsy, and Alzheimer's disease (AD) (Greene et al., 2022; Kyrtata et al., 2021; Nelson et al., 2016; Zilberter and Zilberter, 2017). Patients with Alzheimer's disease (AD) show significantly reduced endothelial glucose transporter levels, reduced glucose transport, and overall brain glucose hypometabolism (Kyrtata et al., 2021). In vitro studies show that BMECs treated with Aβ42, a major component of amyloid plaques in AD, have decreased glucose uptake and glycolytic activity (Raut et al., 2022). These findings suggest that brain vascular defects are significant contributory and perhaps even precipitating factors in neurodegeneration.

While numerous studies have shown endothelial dysfunction in common neurodegenerative diseases, little is known about BMEC function in rare neurogenetic diseases. Niemann-Pick Disease Type C

* Corresponding author at: 8278 Paint Branch Dr., College Park, MD 20742, United States of America.
E-mail address: aclyne@umd.edu (A.M. Clyne).

https://doi.org/10.1016/j.nbd.2024.106769
Received 21 May 2024; Received in revised form 7 December 2024; Accepted 11 December 2024
Available online 18 December 2024

(NP-C) is a rare autosomal recessive disorder caused by mutations in the intracellular cholesterol trafficking proteins NPC1 (95 % of cases) and NPC2 (5 % of cases). These mutations lead to endolysosomal cholesterol accumulation, which is accompanied by cholesterol depletion in the plasma membrane and in organelles such as the endoplasmic reticulum (Vanier, 2010). NP-C is particularly interesting, since NP-C is associated with key AD biomarkers such as APOE ε4, Aβ40 and Aβ42; *NPC1* mutations are implicated in AD (Kresojević et al., 2014); and brain glucose hypometabolism has also been observed in NP-C (Daulatzai, 2017; Kao et al., 2021; Lau et al., 2021; Mosconi et al., 2008). Despite the pathological overlap between these two diseases and recognition of vascular defects in AD pathogenesis, no study has yet examined BMEC function in Niemann-Pick Disease.

Biochemically, NP-C is a disorder of intracellular cholesterol trafficking and sequestration. Cholesterol is crucial to mammalian cell function and its production must be tightly regulated. Cholesterol is sensed primarily by the sterol regulatory element-binding proteins (SREBPs), which then drive cholesterol synthesis through downstream signaling cascades (Horton et al., 2002). Increased cholesterol production alters the metabolic landscape since cholesterol production is an energetically expensive process. A cholesterol compensatory state may upregulate pathways that drive formation of acetyl-CoA (from glycolysis or fatty acid oxidation) and NADPH (from the pentose phosphate pathway; PPP) to supply substrates for cholesterol biosynthesis. This compensation may compromise other metabolic pathways and metabolite transport. NPC1 deficiency triggers this compensatory pathway due to low cholesterol levels in the ER (Lamri et al., 2018). NPC1 inhibition in mouse microglia and Chinese hamster ovary (CHO) cells led to compensatory endogenous cholesterol overproduction accompanied by increased glycolytic gene expression, lactate secretion, and impaired pyruvate decarboxylation and mitochondrial transport (Beltroy et al., 2005; Cougnoux et al., 2018; Kennedy et al., 2013). NPC1 inhibition in BMEC may increase glucose metabolism to fuel compensatory cholesterol biosynthesis, thus reducing glucose availability in the brain.

Disruption of a single metabolic reaction in NP-C and other rare inherited metabolic disorders can lead to systemic changes in the complex, interconnected intracellular metabolic network (Moiz et al., 2021). Assessing these system-wide changes can be difficult in mammalian cells due to the numerous reversible, cyclic, and intertwined metabolic pathways. Isotope-assisted metabolic flux analysis (iMFA) offers a powerful approach to quantify fluxes throughout a metabolic network by combining network models with isotope labeling experiments and extracellular measurements (Moiz et al., 2022). iMFA models are particularly well-suited for the study of monogenic disorders, as they predict how a single genetic perturbation alters the entire metabolic landscape. Previous iMFA models were used to decipher oncogenic metabolic reprogramming incurred by citrate transport protein (Jiang et al., 2017) and fumarate hydratase (Noguchi et al., 2020) genetic deficiency. However, the potential of this approach in studying rare neurogenetic diseases such as NP-C remains untapped.

We therefore investigated how disruption of intracellular cholesterol trafficking with the NPC1 inhibitor U18666A altered BMEC metabolism and glucose availability. We first differentiated iPSCs into BMEC-like cells (hiBMEC) and confirmed that they expressed key properties of brain endothelium. We then examined how treating hiBMEC with the NPC1 inhibitor U18666A affected cholesterol localization, cell viability, and cholesterol biosynthetic factors. We measured the impact of U18666A on glycolytic metabolism via extracellular flux measurements, reverse transcriptase polymerase chain reaction (RT-PCR), heavy isotope tracer labeling, and liquid chromatography mass spectrometry (LC-MS). Using instationary metabolic flux analysis (INST-MFA), an iMFA approach for experimental systems that do not reach isotopic steady state, we estimated intracellular fluxes to further scrutinize changes throughout the metabolic network. We then validated the INST-MFA model estimates through downstream assays and qualitative tracer analysis. We also confirmed several of these metabolic changes in human primary BMECs (hpBMEC), an alternative in vitro BMEC model. Finally, we tested whether treating hiBMEC with hydroxypropyl-β-cyclodextrin (HPβCD), a potential therapeutic for NP-C that releases trapped lysosomal cholesterol (Hammond et al., 2019), could attenuate U18666A-induced metabolic changes. Our results highlight the utility of iMFA for studying rare neurogenetic diseases as well as a potential mechanism through which BMEC may alter glucose availability and potentially whole brain metabolism.

2. Materials and methods

2.1. Cell culture

IMR90 iPSCs (WiCell; provided as a generous gift from Dr. Xiaoming He), which were derived from fibroblasts isolated from the lung tissue of a 16-week old human female, were used to derive BMEC-like cells (hiBMEC) (Yu et al., 2007). IMR90 iPSCs were maintained in mTeSR-Plus medium (STEMCELL Technologies, 100–0276) on Matrigel (Corning, 354,230) coated plates and passaged at 70 % confluence using Versene (Thermo Fisher, 15,040,066). iPSCs were differentiated into BMEC-like cells (hiBMEC) following previously established protocols (Neal et al., 2019). Briefly, iPSC were detached using Accutase (Thermo Fisher, A1110501) and seeded at 200,000 cells/well on Matrigel-coated plates in mTESR-Plus medium supplemented with 10 μM Y27632 (Torcis, 1254). The next day, the medium was changed to E6 (STEMCELL Technologies, 05946), after which medium was replaced every 24 h for four days. On the fifth day, the medium was changed to human endothelial cell serum-free medium (hESFM; Thermo Fisher, 11,111,044) supplemented with 2 % B27 (Thermo Fisher, 17,504,001), 20 ng/mL basic fibroblast growth factor (bFGF; Peprotech, 100-18B), and 10 μM retinoic acid (RA; Millipore Sigma, R2625) for two days.

Cells were then detached with Accutase and subcultured at 1×10^6 cells/cm^2 on plates or Transwell inserts coated with an extracellular matrix (ECM) solution comprised of 0.4 mg/mL collagen IV (Millipore Sigma, C7521) and 0.1 mg/mL fibronectin (Millipore Sigma, F2006) in water. hiBMEC were cultured in hESFM supplemented with 2 % B27, 20 ng/mL bFGF, and 10 μM RA. 24 h after subculture, hiBMEC were changed to hESFM supplemented with 2 % B27.

Human primary BMEC (hpBMEC; Cell Systems, ACBRWE 376 V), which were derived from a male pediatric donor, from were maintained in Endothelial Growth Medium 2-microvascular (EGM2-MV; Lonza, CC-4147) supplemented with 1 % penicillin-streptomycin (Thermo Fisher, 15,140,163), 1 % L-glutamine (Thermo Fisher, 25–030-081), and 10 % fetal bovine serum (FBS; Cytiva, SH30088.03) and used through passage 9.

All experimental treatments were prepared in neurobasal medium (Thermo Fisher; A2477501) containing 8.5 mM glucose, 4.5 mM glutamine, and 2 % B27. Cells were then treated with medium containing U18666A (Sigma-Aldrich, U3633), 1000 μM 2-hydroxypropyl-β-cyclodextrin (HPβCD; Roquette, 128,446), or equivalent volume of phosphate buffered saline (PBS) as the vehicle control (VC).

2.2. Cell viability

Cell viability after U18666A treatment was assessed using a Live/Dead assay (Thermo Fisher, L3224) as per manufacturer's instructions. Briefly, cells were incubated with 4 μM ethidium homodimer (EtHd) and 1 μM Calcein-AM in hESFM with 2 % B27 for 30 min. Methanol-treated cells were used as a positive control for cell death. After washing, media was replaced, and cells were imaged using an Echo Revolve microscope with a 20× objective. The number of calcein-positive and EtHd-positive cells was then counted using ImageJ. Specifically, each image was background corrected, thresholded to create a binary image, and then subjected to the watershed tool to separate cells in close physical proximity. Each individual cell was then considered a particle and counted using the Analyze Particles tool in ImageJ. The number of

calcein-positive cells was divided by total cell count to determine the percentage of live cells.

2.3. Extracellular metabolic measurements

A YSI 2950 Bioanalyzer (Yellow Springs Instruments, 527,690) was used to measure extracellular glucose, lactate, glutamine, and glutamate concentrations. For well plate studies, media samples (200 μL) were collected at specified time points during the experiment. Metabolite uptake or secretion was calculated as the difference in extracellular metabolite concentrations at 0- and 24-h. For Transwell studies, hiBMEC were subcultured on Transwell inserts and cultured for another 48 h until terminally differentiated. Cells were then treated for 48 h, after which 200 μL media samples were collected from both the apical and basolateral compartments for analysis.

2.4. CRISPR-Cas9 NPC1 knock out

NPC1 knockout (NPC-KO) iPSCs were generated by CRISPR/Cas9 through targeting exon 6 of the NPC1 gene using small guide RNA (ACGCCAUGUAUGUCAUCAUG; Synthego), as described previously (Jia et al., 2023). iPSCs were detached with Accutase and resuspended in 100 μL Resuspension Buffer R (Thermo Fisher, MPK10096) at 13.5×10^6 cells/mL with 30 μM small guide RNA and Cas9. Cells were then electroporated for two pulses at 1100 V, 30 millisecond pulse width. Transfected cells were pipetted onto Matrigel coated plates in mTeSR-Plus media with 10 μM Y-27632 and cultured until 70 % confluent.

iPSCs were then dissociated into a single cell suspension with Accutase and seeded sparsely onto a six well plate. Single colonies were picked off with a sterile pipette, transferred into 24-well plates, and cultured until confluent. Each clonal colony was then split into three wells for cryogenic preservation in Cryostore freezing media (StemCell), DNA analysis by Sanger sequencing (GeneWiz), and protein validation by Western blot. Primers used for Sanger Sequencing are listed in Table 1. Sanger sequencing (scored with ICE software) and Western blot were used to confirm knockouts, and phenotypic validation was performed with a filipin immunofluorescence assay. The knockout line used for this study had a 100 % knockout score by Sanger sequencing, did not show an NPC1 band on Western blot, and colocalized filipin with lysotracker by immunofluorescence. The transfected wild-type control had a 6 % knockout score, showed an NPC1 band on Western blot, and localized most filipin to the cell membrane.

2.5. Western blot

To analyze NPC1 protein, cells were lysed in RIPA buffer (ThermoFisher Scientific, 89,901) supplemented with Halt Protease and Phosphatase Inhibitor (ThermoFisher Scientific, PI78440). Protein concentration was quantified via BCA assay (ThermoFisher Scientific, 23,225). Normalized protein samples, sample buffer (ThermoFisher Scientific, NP0008) and reducing agent (ThermoFisher Scientific, NP0009) were combined, boiled at 70 °C for 5 min, and then separated using 4–12 % Bis-Tris gels (ThermoFisher Scientific, NP0323). Proteins were transferred to PVDF (ThermoFisher Scientific, IB24001) or nitrocellulose membranes (ThermoFisher Scientific, IB23001) using an iBlot2 (ThermoFisher Scientific, IBL21001). Membranes were then blocked for 1 h in 5 % bovine serum albumin in PBS containing 0.5 % Tween 20 (ThermoFisher Scientific, 85,113) to reduce non-specific binding. Membranes were incubated in primary antibodies for β-actin (Santa Cruz Biotechnology, sc-47,778) and NPC1 (Novus Biologicals, NB400–148) followed by 2 h in the respective horseradish peroxidase conjugated-secondary antibody. Protein bands were imaged using an Alpha Innotech Fluorchem Imager (Protein Simple). Band intensities were analyzed using AlphaView software.

Table 1
Primer sequences for guide strands.

Primer	Sequence
Forward	5′-CCCTACGCGCAAGTTTATTG-3′
Reverse	5′-CATGCAATGGTATTCATGGAG-3′

2.6. RT-PCR

RNA was isolated from hiBMEC using an RNEasy Mini Kit (Qiagen), quantified on a Nanodrop 2000c (Thermo Fisher), and reverse-transcribed to cDNA using a High-Capacity cDNA Reverse Transcription kit (Thermo Fisher) and a ProFlex Thermal Cycler (Thermo Fisher). qPCR was performed using a QuantStudio 7 Flex qPCR System (Thermo Fisher), with primers for G6PDH (Hs00166169_m1), SREBF1 (Hs02561944_s1), HMGCR (Hs00168352_m1), SREBF2 (Hs01081784_m1), LDHA (Hs01378790_g1), PFKP (Hs00737347_m1) and HK2 (Hs00606086_m1). RPLP0, a ribosomal protein, was used as the housekeeper gene (Hs00420895_gH; all from Thermo Fisher). RT-PCR data were analyzed using the comparative CT method.

2.7. Isotope labeling and mass spectrometry

For isotope labeling experiments, hiBMEC were pretreated with 0 or 10 μM U18666A for 24 h to achieve metabolic steady-state. Cells were then then washed with PBS, and media was replaced with neurobasal media supplemented with ^{13}C labeled metabolites. Labeling media contained 8.5 mM glucose, 4.5 mM glutamine, and 2 % B27.

For isotopically nonstationary metabolic flux analysis (INST-MFA), hiBMEC were labeled for 10 min, 1 h, 4 h, 12 h, or 24 h with [1,2-$^{13}C_2$] glucose (Cambridge Isotope Laboratories, CLM-504-PK). For steady-state analysis, hpBMEC were labeled for 24 h with [U-$^{13}C_6$]glucose (Cambridge Isotope Laboratories CLM-1396). At the end of the labeling period, cell culture media was collected. Cells were lysed with ice cold 80:20 methanol for 15 min at −80 °C, and then scraped, vortexed, and centrifuged to pellet proteins. The protein pellets were air dried and resuspended in RIPA buffer (Thermo Fisher, 89,901). A bicinchoninic acid (BCA) protein assay kit (Thermo Fisher, 23,225) was used to quantify protein concentration. Ion abundance was normalized to the protein concentration.

Metabolites from media and cells were quantified by the University of Colorado School of Medicine Metabolomics Core following previously established protocols (Nemkov et al., 2017). Briefly, 8 μL of each sample was injected into a Q Exactive mass spectrometer (MS) in a randomized order by a Vanquish ultra-high performance liquid chromatograph (UHPLC; Thermo Fisher). Eluent was introduced to the MS through electrospray ionization, and the MS was set to scan in full MS mode (2 mscans) over 65–950 *m/z*. After every ten samples, technical mixes were injected to validate instrument stability (Nemkov et al., 2019). Metabolites were manually annotated and integrated with the KEGG database and Maven (Clasquin et al., 2012; Melamud et al., 2010). Blanks, technical mixes, and ^{13}C natural abundance were used to determine peak quality (Nemkov et al., 2015), and the IsoCor Python package (Millard et al., 2019) was used to correct the isotope labeling. Metaboanalyst 5.0 was used to analyze data and perform Partial-Least Squares-Discriminant Analysis (PLS-DA) and principal component analysis (PCA), calculate variable importance in project (VIP) scores, and perform *t*-tests with false discovery rate correction (Pang et al., 2022).

For sterol analysis, sample extracts were randomized and 8 μL of each sample was injected into a Q Exactive MS by a Vanquish UHPLC using an ACQUITY UPLC HSS T3 column (150 × 2.1 mm, 1.8 μM, Waters) over a 17-min gradient in positive mode, as previously described (Reisz et al., 2019). Atmospheric pressure chemical ionization was used to introduce eluent to the MS which scanned in full MS mode (1 μscans) over the range of 150–1500 *m/z*. Technical mixes were injected every ten samples to determine instrument stability (Reisz et al., 2019).

2.8. Metabolic flux analysis

Isotope assisted metabolic flux analysis (iMFA) was performed in INCA 2.0 (Rahim et al., 2022) using a modified version of the core network we previously described (Moiz et al., 2021). The metabolic map was expanded to include glutathione and GABA synthesis from glutamate, as well as an influx of undiluted aspartate. External metabolite flux rates for glutamate, glutamine, glucose, and lactate were converted into nmol/h for each metabolite according to the following formula:

$$Flux\ Rate\left(\frac{nmol}{hr}\right) = 1000^{*}V^{*}\frac{dC}{dt} \quad (1)$$

where V is media volume in each well (mL), dC is the concentration change from 0 to 24 h (mmol/L), and dt is the time period (hours).

INST-MFA provides additional precision, particularly for reversible and cyclic fluxes, which sometimes cannot be accurately deciphered with steady-state iMFA. For these reasons, we used INST-MFA to analyze the [1,2-$^{13}C_2$] glucose labeled hiBMEC data from five different time points (10 min, 1 h, 4 h, 12 h, and 24 h). We then used the "Estimate Fluxes" module in INCA to fit the model and estimate flux values. INCA uses a Levenberg–Marquardt gradient descent algorithm to estimate fluxes that best account for the measured isotope labeling and extracellular flux data. Simulations were repeated 100 times to improve the odds of finding the global optimum, each time beginning from a random initial point. The goodness of fit was based on the assumption that the minimized sum-of-squared-residuals (SSR) follows a chi-square distribution. The chi-square statistic can be used to determine whether the frequency of observations differs significantly from their frequencies. The chi-square function is defined as:

$$X^2 = \frac{\sum (O_i - E_i)^2}{E_i} \quad (2)$$

where O_i is the isotopomer abundance simulated from the best-fit flux distribution for the ith mass isotopomer and E_i is the experimentally measured abundance of the ith mass isotopomer. The acceptable fit was based on the n–p degrees of freedom, where n is the number of independent measurements and p is the number of fitted parameters. The acceptable SSR range was determined from is:

$$\chi^2_{\alpha/2}(n-p), \chi^2_{\left(1-\frac{\alpha}{2}\right)}(n-p) \quad (3)$$

where α is defined as the acceptable threshold value (Chernoff and Lehmann, 2012). In our study, we set $\alpha = 0.05$ to designate 95 % confidence intervals as the acceptable threshold. All metabolites were set to a minimum error of 1 % as recommended for LC-MS data (Antoniewicz, 2018). To adequately fit the model and prevent either over- or underfitting, we examined residual errors for each isotopomer after each analysis. Any gross outliers that skewed the distribution were rescaled to ensure a relatively normal distribution of residual error. This adjustment process was repeated until the distribution of residuals appeared to be near normal.

Metabolites that produced large model errors (SSR > 150) or showed labeling states that could not be explained by biochemically feasible reactions were designated as erroneous and removed from the model. The final ^{13}C INST-MFA model for VC-treated iPSC-BMECs consisted of 67 reactions with 539 degrees of freedom and fit with an SSR value of 509 (95 % CI = 476.6 to 605.2). The final ^{13}C INST-MFA model for U18666A-treated iPSC-BMECs consisted of 67 reactions with 506 degrees of freedom and fit with an SSR value of 508.8 (95 % CI = 445.6 to 570.2). A full metabolic model description is provided in Supplementary Data 1. For each flux, 95 % confidence intervals were generated using parameter continuation. Fluxes with non-overlapping confidence intervals were considered to be statistically significantly different.

2.9. Seahorse metabolic assays

BMEC oxygen consumption rate (OCR) was measured using the Seahorse Mito Stress Test (Agilent, 103,015–100) while glycolytic proton efflux rate (GlycoPER) was measuring using the Seahorse Glycolytic Rate Assay (Agilent, 103,344–100). On the day of the assay, media was changed to Seahorse DMEM (Agilent, 103,680–100) supplemented with 5.5 mM glucose, 1 mM pyruvate, and 4.5 mM glutamine for 1 h. For the Mito Stress Test, the loading cartridge was prepared to inject oligomycin (1.5 μM), FCCP (0.5 μM), and rotenone + antimycin A (0.5 μM). To measure glycoPER, the cartridge was instead prepared with rotenone + antimycin A (0.5 μM) and 50 mM 2-deoxyglucose. Drug injection and metabolic rate measurements were conducted with a Seahorse XF96 (Agilent) and analyzed using Seahorse Analytics software. Seahorse assay outputs were then normalized to nuclei number. Metabolic rates were then measured using a Seahorse XF96 (Agilent) and analyzed using Seahorse analytics software. Basal mitochondrial respiration values were calculated by subtracting the minimum OCR following R/AA injection from the last OCR value prior to oligomycin injection. After each experiment, cells were fixed with 4 % paraformaldehyde, and nuclei were stained with DAPI (1:1000). Four quadrants of each well were imaged using a Nikon Eclipse 2Ti with a 10× objective, and the nuclei numbers from each quadrant were summed to determine the number of cells per well. Seahorse assay outputs were then normalized to cell number.

2.10. Mitochondrial membrane potential and mitochondrial calcium

Tetramethylrhodamine (TMRM) was used to analyze mitochondrial membrane potential. Cells were seeded into individual 35 mm glass-bottom dishes and cultured to confluence. Cells were then treated with 10 μM U18666A for 24 h in neurobasal media supplemented with 2 % B27. After 24 h, the media was removed and replaced with neurobasal media containing TMRM (1:1000; Sigma-Aldrich T1162), Mitotracker Green FM (1:5000; Thermo Fisher, M7514), and Hoescht (1:2000, nuclei, Thermo Fisher, 33,342) for 30 min. The labeling media was then aspirated and fresh neurobasal media with 2 % B27 was added for 30 min prior to imaging to quench extracellular TMRM. Cells were then imaged on a Nikon Eclipse T2i in a live cell imaging chamber at 37 °C and 5 % CO_2 using a 60× oil objective. Mitotracker was used to confirm that TMRM signal was in the mitochondria. Following imaging, cells were treated with carbonyl cyanide *m*-chlorophenyl hydrazone (CCCP), which opens the mitochondrial permeability transition pore leading to loss of mitochondrial TMRM, to confirm that TMRM was specific for mitochondrial membrane potential.

2.11. Immunofluorescent microscopy

To visualize tight junctions, hiBMEC were fixed in either ice-cold methanol or 4 % paraformaldehyde, depending on manufacturer's recommendations Table 2, for 20 min and then blocked immediately with 5 % donkey serum (Sigma Aldrich, S30-100 mL) in PBS (Thermo Fisher, 70,011,069) for one hour. For paraformaldehyde-fixed cells, the blocking solution was supplemented with 0.2 % Triton X-100 (Alfa Aesar, A16046) to permeabilize cells. Cells were then incubated with primary antibodies (Table 2) overnight at 4 °C. After thorough washing, cells were labeled with the appropriate secondary antibodies (1:200) and washed 3 times before imaging. Samples were imaged on a Nikon 2Ti Eclipse microscope with a 60× oil in confocal mode.

2.12. Statistical analysis

Statistics were analyzed in GraphPad Prism. Non-parametric Mann-Whitney tests were used to compare two unpaired datasets. One-way ANOVA was used to compare multiple groups, followed by post hoc Sidak's multiple comparison test. For time course comparisons,

Table 2
Primary and secondary antibodies.

Target	Primary antibody	Fixation	Primary Antibody Dilution	Secondary antibody (Diluted at 1:200)
Claudin5	Thermo Fisher, 4C3C2	Methanol	1:50	Donkey-anti Mouse 488 (Thermo Fisher, A-21202)
ZO1	Cell Signaling, 13663S	PFA	1:50	Donkey-Anti Rabbit 488 (Thermo Fisher, A-21206)
Occludin	Cell Signaling, 13663S	Methanol	1:50	Donkey-Anti Rabbit 488 (Thermo Fisher, A-21206)
LAMP1	Abcam, ab24170	PFA	1:200	Donkey anti-Rabbit (Thermo Fisher, A-21207)

significance was determined by 2-way ANOVA followed by two-stage linear step-up procedure of Benjamini, Krieger, and Yekutieli to correct for multiple comparisons. We conducted our isotope labeling experiment once but sampled across five different time points. Western blot and total ion count measurements via LC-MS were repeated twice and pooled for analysis. All other experiments were repeated at least three times with independent differentiations and then pooled for analysis. Data were considered statistically significant if $p < 0.05$.

3. Results

3.1. U18666A induced an NPC1-like phenotype in hiBMEC without reducing cell viability

We first confirmed that hiBMEC formed a tight barrier and that U18666A treatment altered intracellular cholesterol distribution. hiBMEC cultured on Transwell inserts achieved trans-endothelial electrical resistance (TEER) values from 1700 to 6000 Ohms x cm^2 and formed continuous cell-cell boundaries of key tight junction proteins such as occludin, zonula occludens-1 (ZO-1), and claudin-5. (Supplemental Fig. 1A,1B). Endolysosomal cholesterol accumulation, as indicated by filipin staining, occurred at 5 and 10 μM U18666A (Supplemental Fig. 1C). U18666A can have off-target effects, including decreased cholesterol biosynthesis through inhibition of 3β-hydroxysterol Δ-24-reductase (DHCR24), an enzyme that reduces desmosterol into cholesterol (Cenedella, 2009). We did not observe a change in desmosterol in U18666A-treated hiBMEC via mass spectrometry (Supplemental Fig. 1D (Cenedella, 2009). We did not observe a change in desmosterol, a cholesterol synthesis intermediate, in U18666A-treated hiBMEC via mass spectrometry (Supplemental Fig. 1D).

3.2. U18666A increased hiBMEC glycolytic metabolism

Previous work indicates that NPC1 deficiency increases glycolytic activity in microglia and CHO cells (Kennedy et al., 2014; Kennedy et al., 2013). We therefore examined how U18666A impacted hiBMEC glycolytic metabolism by measuring glucose and lactate extracellular fluxes. Both glucose uptake and lactate secretion increased in a dose-dependent manner with U18666A (Fig. 1A). At 10 μM U18666A, glucose uptake increased by nearly 33 % ($p < 0.0009$) and lactate secretion by ~38 % ($p < 0.0001$). Once inside the cell, glucose can be metabolized into lactate via anaerobic glycolysis, diverted into side branch pathways, or routed to the mitochondria as pyruvate for oxidative phosphorylation. The lactate:glucose ratio indicates whether there are changes in glucose metabolism, as increased intracellular utilization can diminish lactate secretion. The lactate:glucose ratio did not change in U18666A-treated hiBMEC.

We then quantified U18666A-treated hiBMEC gene expression by RT-PCR to determine if the observed increase in glycolysis with

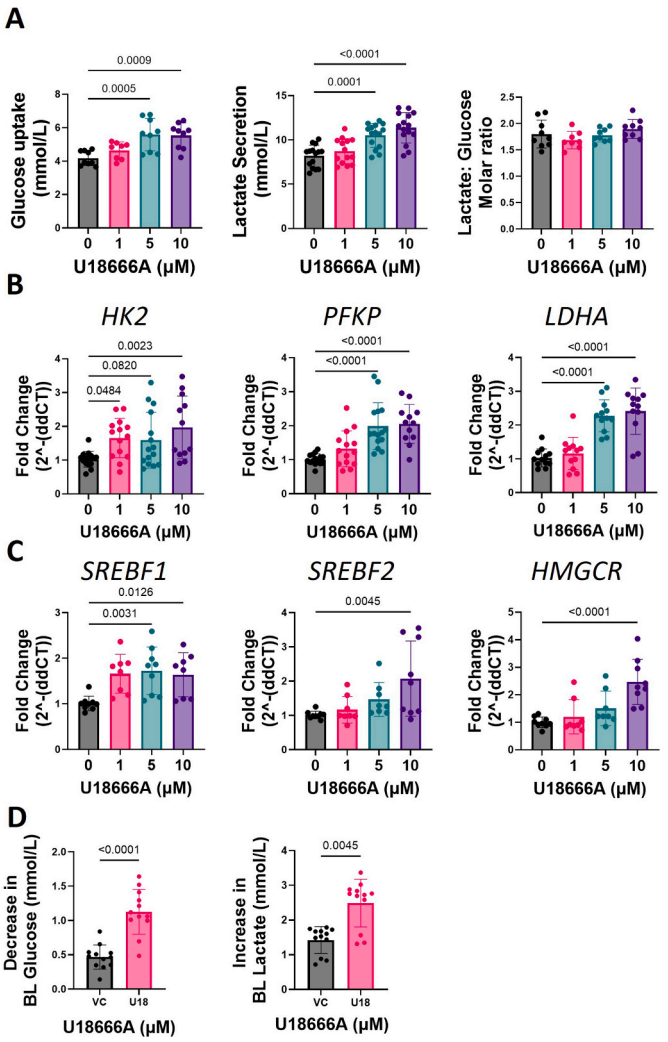

Fig. 1. U18666A increased glycolysis and cholesterol biosynthesis in hiBMEC. (A) Glucose uptake, lactate secretion, and lactate:glucose ratio following hiBMEC treatment with 0, 1, 5, or 10 μM U18666A for 48 h, measured with a YSI bioanalyzer (n = 9–16 samples, 3–4 independent experiments). (B) Gene expression fold change for the glycolytic rate-limiting enzymes hexokinase 2 (HK2), phosphofructokinase platelet isoform (PFKP), and lactate dehydrogenase A (LDHA), measured by RT-PCR (n = 9–12 samples, 3–4 independent experiments). (C) Gene expression fold change for sterol regulatory binding elements 1 and 2 (SREBF1/SREBF2) and HMG-CoA Reductase (HMGCR), measured by RT-PCR (n = 7–9, 3 independent experiments). Each data point was normalized to the mean of the 0 μM U18666A group for each experiment. (D) Change in total basolateral glucose and lactate concentrations following treatment with U18666A (U18) or vehicle control (VC) for 48 h (n = 12, 3 independent experiments). Data are shown as mean +/− standard deviation. Statistical significance among multiple groups determined by Kruskal-Willis non-parametric test followed by Dunn's multiple comparison test.

U18666A treatment related to changes in rate-limiting glycolytic enzymes such as hexokinase 2 (*HK2*), phosphofructokinase (*PFKP*), and lactate dehydrogenase (*LDHA*) (Fig. 1B). HK2, which catalyzes glucose phosphorylation to glucose-6-phosphate (G6P), increased in a dose-dependent manner with U18666A treatment, with a maximum increase of 1.97-fold at 10 μM U18666A ($p = 0.0023$). *PFKP*, which catalyzes fructose-6-phosphate (F6P) phosphorylation into fructose-1-6-biphosphate (F16BP), doubled with 5 μM U18666A ($p < 0.0001$) and with 10 μM U18666A ($p < 0.0001$). *LDHA* also increased by 2.27-fold with 5 μM U18666A ($p < 0.0001$) and 2.41-fold with 10 μM U18666A ($p < 0.0001$).

Increased glycolysis can be initiated by sterol regulatory element

binding factors (SREBFs), which are elevated in cholesterol-deplete states (Gosmain et al., 2005; Horton et al., 2002). In addition, NPC1 regulates feedback inhibition of the SREBP pathway, and NPC1 deficiency can lead to increased cholesterol biosynthesis (Lamri et al., 2018). We therefore examined changes in cholesterol biosynthesis gene expression via RT-PCR. 5 and 10 μM U18666A increased *SREBF1* mRNA by 1.73-fold ($p = 0.0031$) and 1.93-fold ($p = 0.0126$), respectively, while 10 μM U18666A significantly increased *SREBF2* mRNA (2.07-fold, $p = 0.0045$). We also observed increased expression of the rate-limiting cholesterol synthesis enzyme HMG-CoA reductase (*HMGCR*) with 10 μM U18666A (2.47-fold, $p < 0.0001$) but did not note significant increases at lower concentrations (Fig. 1C). Together, our results suggest that 10 μM U18666A maximized changes in hiBMEC metabolism, cholesterol accumulation, and cholesterol biosynthesis without loss of cell viability. We therefore used this concentration to model an NPC-like hiBMEC phenotype in subsequent experiments.

In vivo, BMECs are exposed to glucose on their apical and basolateral sides as they integrate glucose metabolism and transport to other brain cells. We therefore measured how increased glycolysis in U18666A-treated hiBMEC altered glucose availability in the basolateral compartment in hiBMEC cultured on Transwell membranes. We found that after 48 h, vehicle control (VC) cells decreased basolateral glucose by 0.51 mmol/L, while U18666A-treated cells decreased basolateral glucose by 1.12 mmol/L ($p < 0.0001$; Fig. 1D). Basolateral lactate levels were 74 % higher in U18666A-treated as compared to VC cells (2.49 vs. 1.43 mmol/L; $p = 0.0045$; Fig. 1D). Thus, NPC1 inhibition decreased basolateral glucose while increasing basolateral lactate.

To determine whether the metabolic changes observed are due to acute pharmacological inhibition, we generated a CRISPR-Cas9 NPC1 knockout iPSC line, which showed abolishment of NPC1 protein and increased cholesterol accumulation (Supplemental Fig. 3A, 3B). YSI analysis of Transwell cultures replicated the significant increases in both apical (~15 %, $p = 0.001010$) and basolateral (13 %, $p = 0.008707$) lactate but did not did not show significant changes in glucose uptake.

3.3. U18666A altered the hiBMEC TCA cycle and PPP metabolome

We then labeled U18666A-treated hiBMEC with [1,2-$^{13}C_2$] glucose to understand intracellular metabolic changes. [1,2-$^{13}C_2$] glucose is useful for determining fluxes at glycolytic branch points, particularly the PPP (Beyß et al., 2021; Jang et al., 2018). PLS-DA showed that samples separated by time point across component 1 for VC cells (PC1 = 44.4 %) and across component 2 for U18666A-treated cells (PC2 = 16.8 %, Fig. 2A). A heat map of the total labeled metabolite fractions showed differences in metabolite labeling, particularly in the TCA cycle and amino acids (Fig. 2B).

To identify isotopomers that distinguished VC from U18666A-treated hiBMEC, we used a VIP plot to rank specific isotopomers (Fig. 2C). The metabolites with the top 15 VIP scores include isotopomers in the PPP such as glyceraldehyde-3-phosphate (GAP; M + 2 and M + 1), F16BP (M + 4 and M + 2), and ribose-5-phosphate (R5P; M + 1 and M + 0). Over representation of PPP-associated metabolites in the VIP plot suggests that differences in these metabolites are consistent across multiple time points, including earlier times when metabolites have not reached isotopic steady state.

3.4. iMFA predicted increased glycolytic side branch pathway flux and decreased mitochondrial metabolism

We next used iMFA to predict intracellular metabolic fluxes based on the LC-MS data. Since isotopic labeling in hiBMEC has not yet been reported, it was essential to determine when the hiBMEC reached metabolic and isotopic steady state. We first quantified extracellular metabolite concentration over time immediately following U18666A treatment (Supplemental Fig. 4). Both VC and U18666A-treated hiBMEC demonstrated a linear change in extracellular metabolite concentrations. U18666A-treated hiBMEC had slightly higher glucose uptake rates (0.24 mmol/L/h, 95 % CI = 0.229–0.259 mmol/L/h) compared to VC hiBMEC (0.20 mmol/L/h, 95 % CI = 0.174–0.229 mmol/L/h). A similar trend was observed for lactate, which was secreted at 0.484 mmol/L/h (95 % CI = 0.458–0.510 mmol/L/h) in U18666A-treated hiBMEC vs. 0.377 mmol/L/h (95 % CI = 0.336–0.418 mmol/L/h) in VC hiBMEC. In contrast, glutamine uptake was not significantly different between the treatment conditions (0.007 mmol/L/h in U18666A-treated hiBMEC vs. 0.005 in VC hiBMEC). Previous work in our lab (Weber et al., 2024) showed that hiBMECs do not secrete glutamate and therefore glutamate secretion was not measured. Together, these data show that hiBMEC were at metabolic steady state 24 h after being treated with U18666A.

To establish when hiBMEC reached isotopic steady state, we quantified the intracellular labeled metabolite fractions of hiBMEC labeled with [1,2-$^{13}C_2$] glucose over five time points following labeling (10 min, 1 h, 4 h, 12 h, and 24 h; Supplemental Fig. 5). Most of the glycolytic, PPP, and TCA cycle metabolites did not significantly change labeling patterns after 12 h, indicating that hiBMEC reached isotopic steady state by 12 h. Together, these data show that our experimental conditions were sufficient to perform steady-state iMFA and INST-MFA in hiBMEC.

The INST-MFA predicted increased glucose flux into glycolysis in U18666A-treated cells (Fig. 3, Supplementary Data 2). There were statistically significant increases in glucose entry into the PPP (1.61-fold), pyruvate generation (1.08-fold), and pyruvate reduction to lactate (1.34-fold) with U18666A treatment. INST-MFA predicted a large but not statistically significant increased flux into the hexosamine biosynthetic pathway (HBP) in U18666A treated cells, primarily because the flux was predicted to be near zero in the VC cells.

INST-MFA also predicted decreased glucose metabolism in the TCA cycle. Pyruvate entry into the TCA cycle decreased to 0.54-fold in U18666A treated cells, which was statistically significant. Other statistically significant differences in the INST-MFA between the VC and U18666A-treated cells involved glutamate. α-ketoglutarate (AKG) was predicted to generate glutamate in U18666A-treated hiBMEC, which was the opposite flux direction of VC hiBMEC. Finally, more glutamate was directed towards glutathione synthesis in U18666A-treated hiBMEC. Together, the INST-MFA model predicted that hiBMEC increased glycolytic metabolism while redirecting intracellular glucose and glutamine away from mitochondrial metabolism.

3.5. Isotope tracer analysis and G6PDH mRNA expression supported INST-MFA PPP flux estimates

To further investigate INST-MFA-predicted changes in the PPP, we examined PPP intermediate isotopomers. [1,2-$^{13}C_2$] glucose forms [M + 2] G6P, which then can enter the PPP to form [M + 1] R5P or xylulose-5-phosphate (X5P). [M + 2] G6P can alternatively enter the gluconeogenic pathway as [M + 2] UDP-glucose or continue down glycolysis to become [M + 2] F16BP. F16BP is formed from phosphorylation of F6P and can therefore be used as a proxy for F6P labeling at metabolic steady-state.

[M + 4] F6P is primarily synthesized from a mixture of [M + 1] R5P, [M + 1] X5P (derived from R5P), and [M + 2] glyceraldehyde (Fig. 4A). Therefore, increased [M + 1] R5P and [M + 4] F16BP, as well as decreased [M + 2] UDP-glucose, indicates increased PPP flux at the G6P branchpoint. Indeed, we observed higher [M + 1] R5P in U18666A-treated cells 1 h post-labeling and at every time point thereafter. Significant differences were found at 12 h (1.23-fold higher, $p = 0.0005$) and 24 h post-labeling (1.50-fold higher, $p < 0.0001$; Fig. 4B). [M + 4] F16BP was similarly consistently higher at all time points in U18666A-treated hiBMEC. At 24 h, [M + 4] F16BP was ~1.7 fold higher in U18666A-treated hiBMEC than in VC cells ($p = 0.0067$; Fig. 4C). [M + 2] UDP-glucose was lower in U18666A treated hiBMEC at nearly all time points, with a significant decrease of ~0.8-fold at 4, 12, and 24 h (Fig. 4D). Finally, we quantified expression of *G6PDH*, the rate-limiting enzyme which controls G6P entry into the PPP. G6PDH mRNA was 26 %

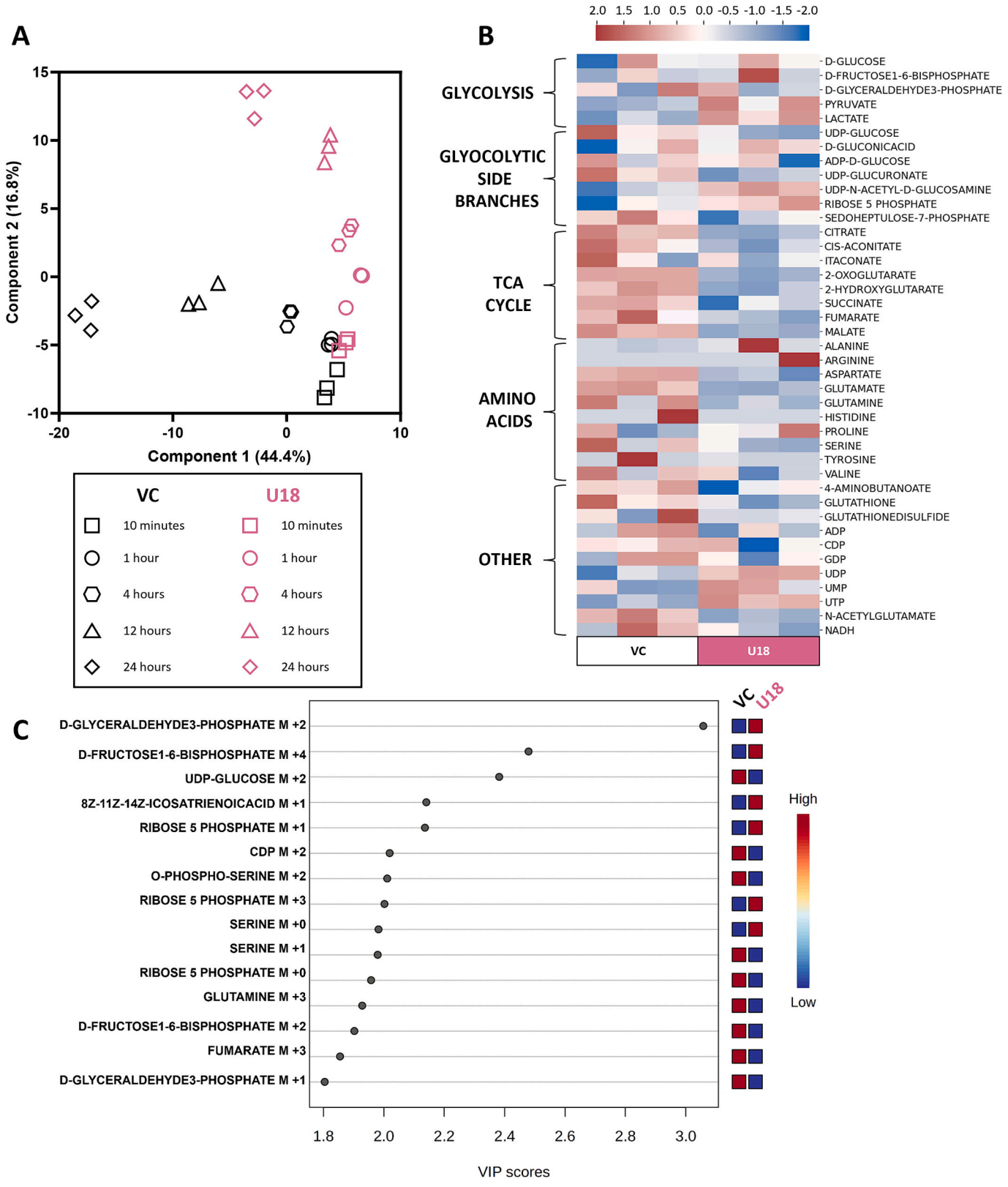

Fig. 2. Isotope labeling showed metabolic differences in the TCA cycle and PPP with U18666A treatment. (A) Partial-least squares discriminant analysis (PLS-DA) from isotopomer data following hiBMEC labeling with [1,2-$^{13}C_2$] glucose from all time points ($n = 3$ samples per time point and treatment). (B) Heatmap showing total labeled fractions at 24 h following hiBMEC labeling with [1,2-$^{13}C_2$] glucose. Each row was normalized using *Z*-score standardization. (C) Variable importance in project (VIP) score plot shows the 15 highest ranking isotopomers that consistently separated between VC and U18666A-treated hiBMEC across all time points.

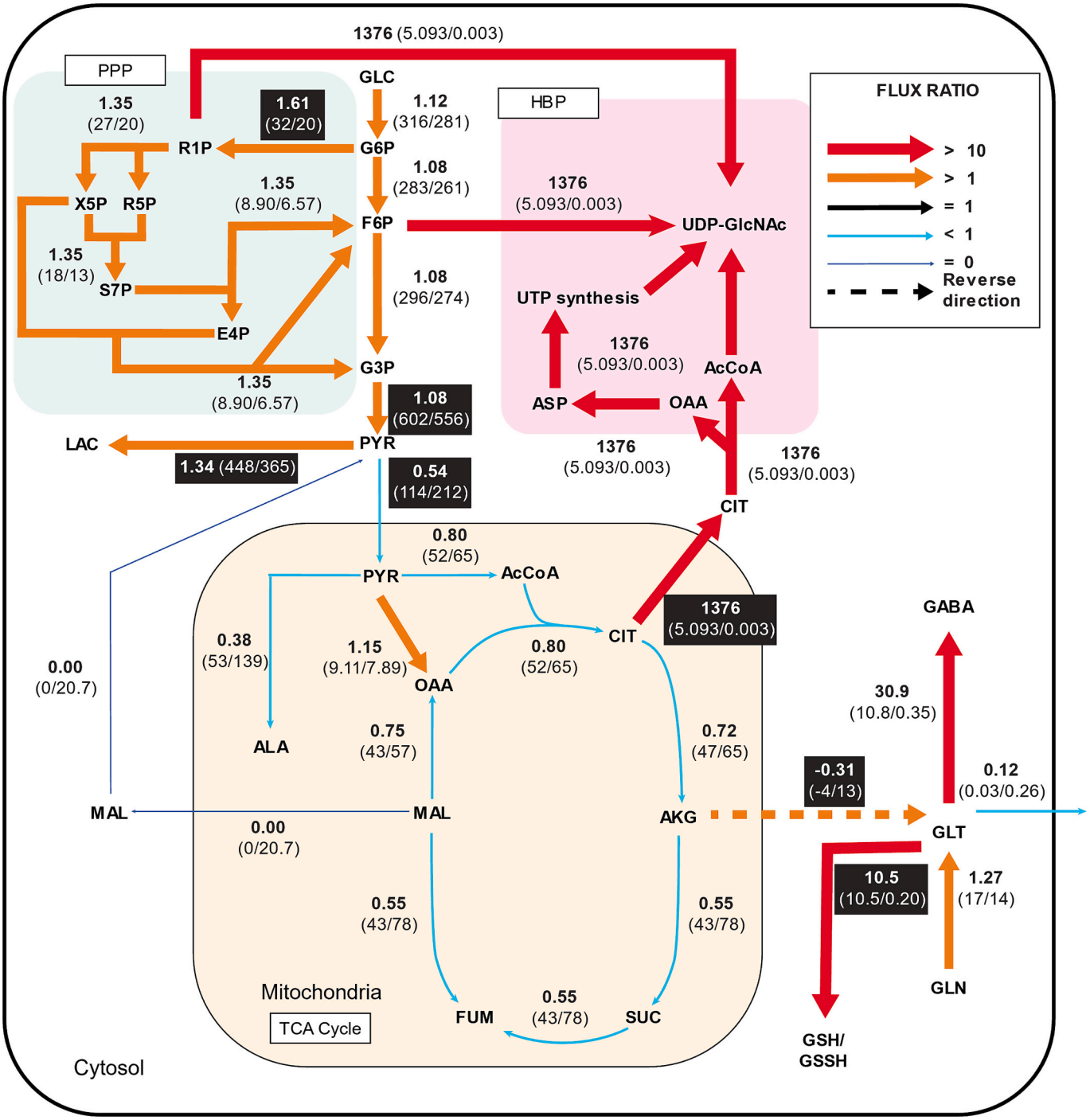

Fig. 3. INST-MFA predicted increased glucose flux in glycolytic side branches but diminished entry into mitochondria. Metabolic flux map for U18666A treated hiBMEC. Arrow thickness and colors indicate relative flux ratio (defined as U18666A-treated flux value/VC flux value). Flux ratios are noted next to arrow, while the absolute flux values from U18666A-treated hiBMEC and VC hiBMEC are shown in parenthesis either next to or underneath the flux ratio. Flux ratios in black boxes indicate reactions where confidence intervals (calculated by parameter continuation in INCA) between U18666A and VC hiBMECs did not overlap. Blue arrows indicate reactions in which U18666A-treated cells had zero or close to zero flux while VC cells were estimated to have non-zero flux. Red arrows indicate reactions where there was at least a 10-fold increase in U18666A-treated hiBMEC. Dashed arrows indicate reactions with reversed net flux direction in U18666A-treated vs VC hiBMEC. (For interpretation of the references to colour in this figure legend, the reader is referred to the web version of this article.)

higher ($p = 0.0019$) in U18666A-treated hiBMEC as compared to VC-treated cells (Fig. 3E). Together, these data suggest that U18666A funnels glucose away from glycogen synthesis and into the PPP via increased G6PDH.

3.6. HBP flux increased in U18666 A-treated hiBMEC labeling even though total UDP-GlcNAc and protein O-GlcNAcylation decreased

We next investigated HBP flux, which was predicted to increase in the INST-MFA model. The HBP branches off glycolysis at F6P and produces uridine-5′-diphospho-*N*-acetylglucosamine (UDP-GlcNAc) via the rate-limiting enzyme glutamine-fructose-6-phosphate transaminase 1

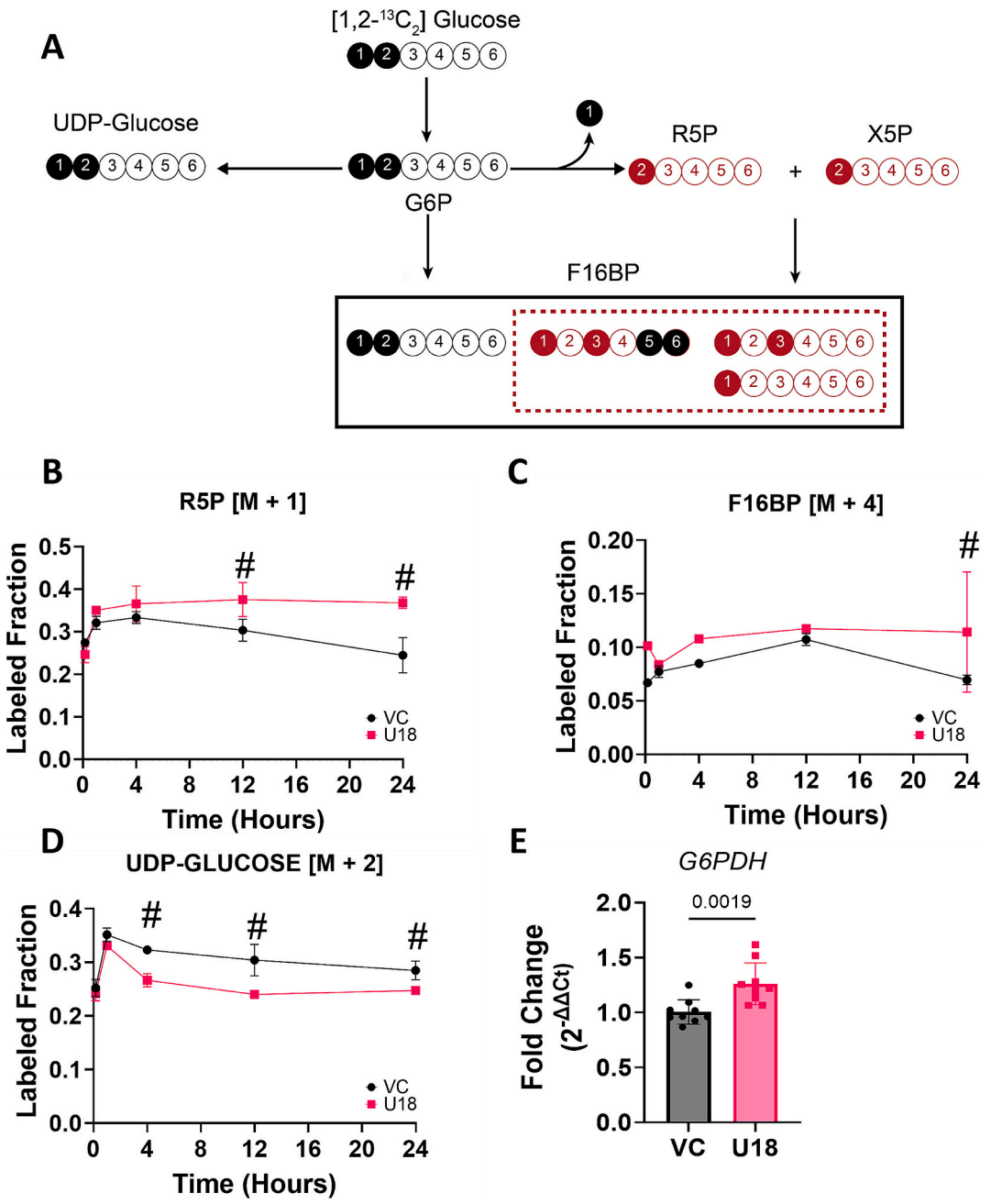

Fig. 4. U18666A increased G6P flux into the PPP, perhaps through increased *G6PDH*. (A) Schematic showing [1,2-$^{13}C_2$] glucose flux at key glycolytic side branch points. [1,2-$^{13}C_2$] glucose is metabolized in glycolysis to [M + 2] glucose-6-phosphate (G6P) and then [M + 2] fructose-1,6-biphosphate (F16BP). When [1,2-$^{13}C_2$] G6P enters the PPP, the first carbon is cleaved, leaving an [M + 1] six carbon sugar that becomes ribose-5-phosphate (R5P) and xylulose-5-phosphate (X5P). In the non-oxidative PPP, [M + 1] R5P and [M + 1] X5P can combine to eventually form [M + 2] F16BP. [M + 4] F16BP is uniquely formed from glycolysis derived [M + 2] glyceraldehyde-3-phosphate (GAP) with PPP-derived [M + 2] F16BP. Therefore, [M + 4] and [M + 1] F16BP can form only from PPP and are measures of glucose entry into the PPP, whereas [M + 2] F16BP can come from glycolysis or the PPP. The F16BP isotopomers that can only be derived from the PPP are designated in the red box. Labeled fractions for (B) [M + 1] R5P (indicative of G6P entry into the PPP), (C) [M + 4] F16BP (unique to PPP), and (D) [M + 2] UDP-Glucose (an alternative route for G6P towards glycogen synthesis). # is used to indicate statistical significance between groups at specified time points ($p < 0.05$) (E) Fold change of *G6PDH* expression in hiBMECs treated with U18666A for 48 h, as measured by RT-PCR ($n = 9$ samples, 3 independent experiments). All data shown as mean +/− standard deviation. Two-way ANOVA and Sidak's MCT used to compare labeled fractions at each time point. Mann-Whitney test used to determine statistical significance when comparing two groups. (For interpretation of the references to colour in this figure legend, the reader is referred to the web version of this article.)

(GFAT1). UDP-GlcNAc is then added to proteins via O-GlcNAc transferase (OGT) to regulate protein function (Paneque et al., 2023). The UDP-GlcNAc labeled fraction was consistently higher in U18666 A-treated hiBMEC by 4 h following the start of our labeling experiment (Fig. 5A). The HBP is inhibited by UDP-GlcNAc, so we questioned whether increased HBP flux related to decreased UDP-GlcNAc. Indeed, U18666A-treatment decreased UDP-GlcNAc pool size by more than 40 % ($p < 0.0001$) (Fig. 5B). Protein O-GlcNAcylation decreased by ~30 % ($p = 0.0649$), while GFAT1 did not change (Fig. 5C). Decreased UDP-GlcNAc levels despite increased flux suggests a compensatory state in which hiBMEC tried to maintain UDP-GlcNAc levels.

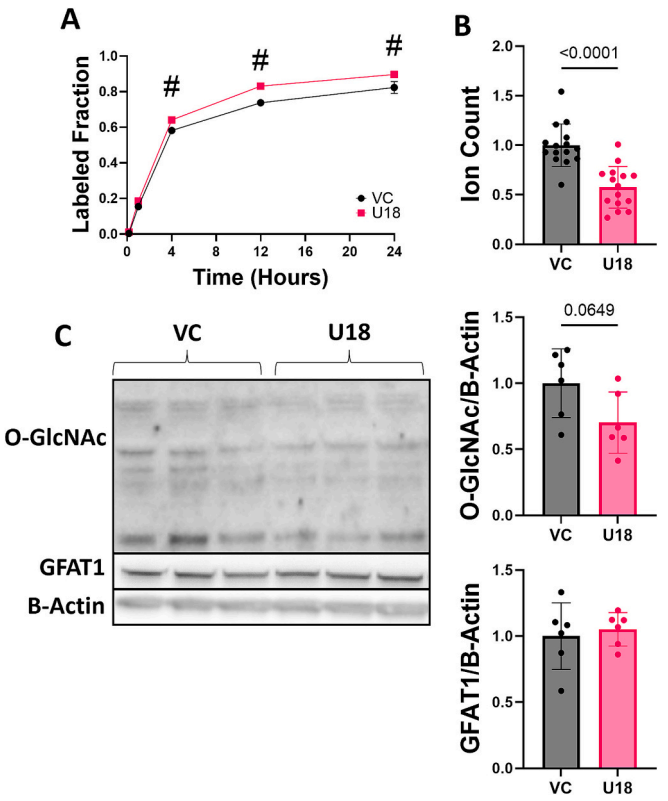

Fig. 5. U18666 A-treated hiBMEC increased UDP-GlcNAc labeling but decreased UDP-GlcNAc ion count and protein O-GlcNAcylation. (A) [1,2-$^{13}C_2$] glucose labeling of UDP-GlcNAc for 0–24 h. Statistical significance between U18666 A-treated and VC hiBMEC for each time point indicated by # ($p < 0.05$). (B) Normalized ion count data for intracellular UDP-GlcNAc pooled from all 5 time points and normalized to the mean of each respective time point ($n = 15$ samples, 3 per time point). (C) Representative Western blots with quantification for UDP-GlcNAc, GFAT, and β-Actin ($n = 6$ samples, 2 independent experiments). All data shown as mean +/− standard deviation. Two-way ANOVA and Sidak's MCT used to compare labeled fractions at each time point. Mann-Whitney test used to determine statistical significance when comparing two groups.

3.7. U18666A decreased hiBMEC and hpBMEC mitochondrial metabolism

We then examined how U18666A affected hiBMEC mitochondrial metabolism, since our INST-MFA also showed decreased glucose and glutamine flux into the TCA cycle. Basal mitochondrial respiration, was nearly 40 % lower ($p < 0.0001$) in U18666A-treated hiBMEC (Fig. 6A, B). Similarly, maximal respiration was ~78 % lower and spare respiratory capacity was nearly 50 % lower with U18666A treatment ($p < 0.0001$; Fig. 6C, D). Tetramethyl rhodamine ester (TMRM), which measures mitochondrial membrane potential, was ~45 % lower in U18666A treated cells (Fig. 6E, F). To determine whether changes in mitochondrial respiration related to reduced influx of glucose-derived carbons into the mitochondria, we examined [1,2-$^{13}C_2$] glucose labeling patterns in U18666A-treated cells. By 4 h and up to 24 h, U18666A-treated hiBMEC had reduced TCA metabolite labeling compared to VC cells. At 24 h, the labeled fractions indicated 0.88-fold less citrate ($p < 0.0001$), 0.66-fold less AKG ($p < 0.0001$), and 0.75-fold less succinate ($p = 0.0171$; Fig. 6G, H).

Decreased fractional enrichment of labeled glucose in TCA metabolites could indicate either decreased TCA metabolite production, as predicted by the INST-MFA, or increased TCA metabolites derived from unlabeled carbon sources (e.g., amino acids, fatty acids). We therefore compared intracellular TCA metabolite pool sizes between VC and U18666A-treated hiBMEC. Citrate ion count decreased by 53 % ($p < 0.0001$), AKG by 39 % ($p < 0.0001$) and succinate by 42 % ($p < 0.0001$) (Fig. 6H). PLS-DA of the total ion counts showed separation of U18666A-treated hiBMEC from VC cells (Supplemental Fig. 6A) along both components. Through a VIP score plot (Supplemental Fig. 6B), we further identified that 7 of the top 20 ranked metabolites were carnitine derivates. Intracellular pool sizes of these carnitines all decreased with U18666A treatment. Specifically, L-carnitine decreased by 25 % ($p = 0.0025$), propionylcarnitine (acyl-C3) decreased by 87 % ($p < 0.0001$), and butrylcarnitine (acyl-C4) decreased by 49 % ($p < 0.0001$) in U18666A-treated hiBMEC (Supplemental Fig. 6C). Carnitines are important to mitochondrial function as they are involved in fatty acid oxidation (Flanagan et al., 2010). These data suggest that U18666A reduced mitochondrial membrane potential and metabolism.

Finally, we investigated whether U18666A-induced metabolic changes also occurred in hpBMEC. U18666A treatment had similar effects in hpBMEC to those observed in the hiBMEC. Specifically, U18666A treatment increased glucose uptake (~7 %, $p = 0.0538$) and lactate secretion (12 %, $p = 0.0527$) with no change in lactate:glucose ratio (Supplemental Fig. 7 A). U18666A-treated hpBMEC also showed approximately 2-fold increase in [M + 6] UDP-GlcNAc when labeled with [U$^{13}C_6$] glucose, along with reduced UDP-GlcNAc ion count (~73 % decrease, $p = 0.0022$; Supplemental Fig. 7B, 7C). We also observed decreased citrate ($p = 0.002186$), glutamate (proxy for AKG, $p = 0.0022$), and succinate ($p = 0.0022$) labeled fractions (Supplemental Fig. 7D), as well as intracellular acyl-C3 (92 % lower; $p = 0.0022$) and acyl-C4 (40 % lower; $p = 0.0389$) in U18666A-treated hpBMEC (Supplemental Fig. 7E). Finally, similar to our observations in hiBMEC, U18666A-treated hpBMEC showed 40 % lower basal OCR ($p < 0.0001$) and a trend towards lower TMRM ($p = 0.0947$; Supplemental Fig. 7F, 7G, 7H).

3.8. HPβCD partially restored metabolic fluxes in U18666A-treated hiBMEC

HPβCD, which releases cholesterol from the lysosome, has been shown to delay disease onset and improve lifespan in animal models as well as slow disease progression in clinical trials (Abi-Mosleh et al., 2009; Hammond et al., 2019; Liu et al., 2009; Sharma et al., 2023). We therefore determined if HPβCD could restore hiBMEC metabolic phenotype after U18666A treatment. We first verified that HPβCD reversed hiBMEC cholesterol disruption. Lysosomal cholesterol accumulation was reduced and *HMGCR* expression decreased by 38 % ($p = 0.0003$) in hiBMEC concurrently treated with U18666A and HPβCD (Supplemental Fig. 8).

We then examined how HPβCD changed the hiBMEC metabolic phenotype induced by U18666A. HPβCD reduced glucose consumption and lactate secretion in U18666A-treated hiBMEC by ~9 % ($p = 0.0008$) and ~ 8 % ($p < 0.0097$), respectively (Fig. 7A). HPβCD co-treatment also attenuated basolateral glucose depletion by ~29 % ($p = 0.0387$) and restored the lactate increase, although this change was not statistically significant (Fig. 7B). Similarly, HPβCD attenuated the U18666A-induced increase in basal glycolysis from 1.61-fold to 1.15-fold ($p = 0.0114$; Fig. 7C, D) and the U18666A-induced decrease in basal OCR from 0.43 to 0.62-fold ($p = 0.0031$; Fig. 7E, F) relative to VC hiBMECs.

3.9. HPβCD partially restored intracellular metabolite abundance in U18666A-treated hiBMEC

Finally, we examined HPβCD effects on intracellular metabolite levels by LC-MS. PCA demonstrated that HPβCD moved the metabolomic profile of U18666A-treated hiBMEC closer to that of VC hiBMEC (PC1 = 21.7 %, Fig. 8A). HPβCD partially restored UDP-GlcNAc (Fig. 8B) as well as TCA metabolites citrate, AKG, and succinate (Figs. 8C-E). L-carnitine (25 % increase, $p = 0.0630$) and propionylcarnitine (2-fold increase, $p = 0.0003$) but not butyrylcarnitine were partially restored

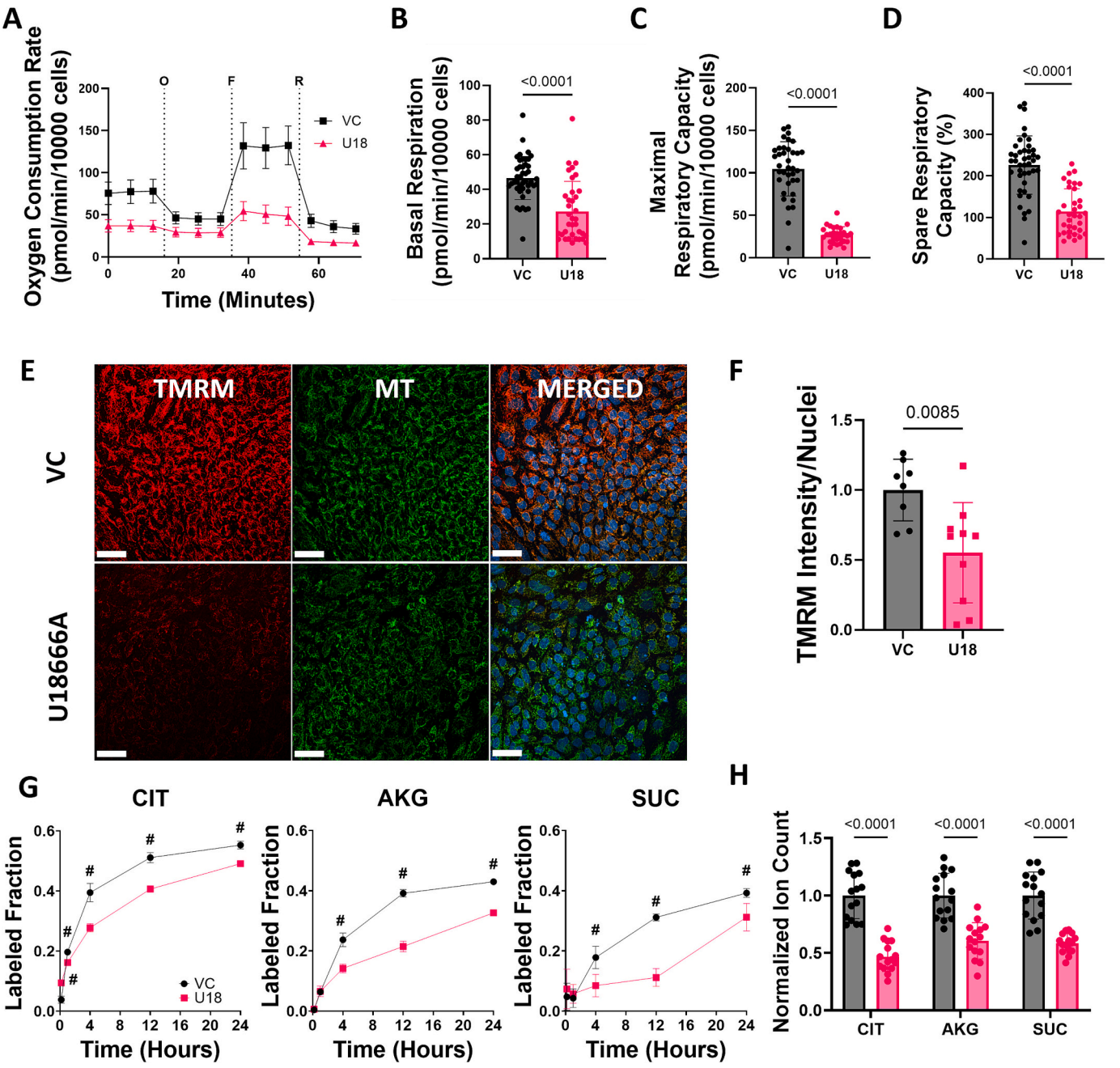

Fig. 6. U18666A-treated hiBMEC demonstrated mitochondrial dysfunction. (A) Representative Seahorse Mitochondrial Stress Test following 24-hour treatment with VC or U18666A. Oligomycin (O), carbonyl p-trifluoro-methoxyphenyl hydrazone (FCCP), and rotenone/antimycin A (R/AA) were injected at specified time points. (E) Representative images of hiBMEC treated with VC or U18666A for 24 h and labeled with tetramethylrhodamine (TMRM; red; mitochondrial potential), Mito-Tracker (MT; green), and (4′,6-diamidino-2-phenylindole) (DAPI; blue; in merged images only). Scale bar = 20 μM. (F) Quantification of TMRM intensity normalized to nuclei count ($n = 9$ samples, 3 independent experiments). (G) Citrate (CIT), α-ketoglutarate (AKG), and succinate (SUC) labeled fractions at 10 min, 1 h, 4 h, 12 h, and 24 h after addition of [$U^{13}C_{1,2}$] glucose, measured by LC-MS. # indicates statistical significance ($p < 0.05$) between groups at each time point. (H) Normalized ion counts for intracellular citrate, α-ketoglutarate, and succinate pooled from all 5 time points and normalized to mean of respective time point ($n = 15$ samples, 3 per time point). Each data point was normalized to mean of VC group for the respective experiment. All data shown as mean +/− standard deviation. Mann-Whitney test used to determine statistical significance when comparing two groups. Two-way ANOVA and Sidak's MCT used to compare labeled fractions at each time point. (For interpretation of the references to colour in this figure legend, the reader is referred to the web version of this article.)

with HPβCD treatment (Supplemental Fig. 9A). NPC1 dysfunction was previously shown to elevate mitochondrial cholesterol in neurons and CHO cells, which can lead to mitochondrial dysfunction (Balboa et al., 2017; Charman et al., 2010; Tiscione et al., 2021). Pregnenelone, which is generated from cholesterol in the inner mitochondrial membrane, increased ~18-fold ($p = 0.0001$) in U18666A-treated cells but decreased to 1.8-fold of VC samples when hiBMEC were co-treated with HPβCD ($p = 0.0001$). Similar patterns were observed for androsterone, a progesterone derivative, and lumisterol, which is derived from 7-dehydrocholesterol (Supplemental Fig. 9B).

4. Discussion

BMECs play a crucial role in maintaining cerebral metabolic

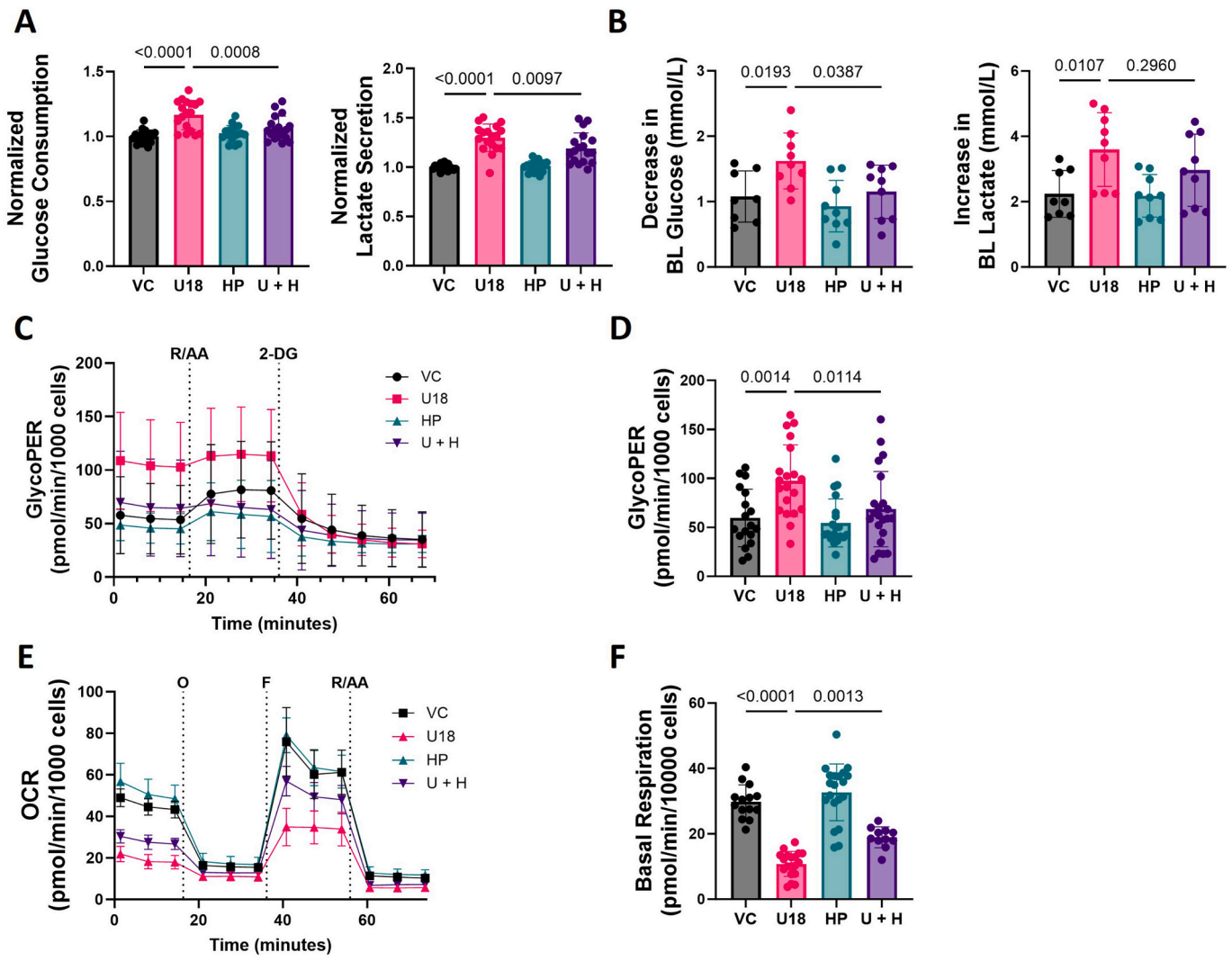

Fig. 7. HPβCD partially restored metabolic fluxes in U18666A-treated hiBMEC. (A) Normalized glucose uptake and lactate secretion following hiBMEC treatment for 48 h with 0 or 10 μM U18666A and 0 or 1000 μM HPβCD, measured with a YSI bioanalyzer (n = 18 samples, 6 independent experiments). Each data point was normalized to the mean of the VC group for each experiment. (B) YSI measurements of glucose and lactate from basolateral compartment of Transwell inserts following 48-h treatment with 0 or 10 μM U18666A and 0 or 1000 μM HPβCD (n = 9 samples, 3 independent experiments). (C) Representative glycolytic proton efflux rate (glycoPER) as quantified by Seahorse GlycoPER assay. Rotenone/antimycin A (R/AA) and 2-Deoxyglucose (2-DG) were injected at specified time intervals. (D) Quantification of basal glycoPER aggregated from Seahorse Glycolytic Rate assays (n = 18–22, 2 independent experiments). All data shown as mean +/− standard deviation. One-way ANOVA followed by Sidak's MCT used to compare multiple groups.

homeostasis by dictating nutrient influx and efflux. Since BMEC metabolism may impact nutrient availability in the brain, it is crucial to evaluate BMEC metabolic phenotypes in neurodegenerative diseases such as NP-C. We now show that the NPC1 inhibitor U18666A increased hiBMEC glycolytic metabolism and flux into glycolytic branch pathways while diminishing mitochondrial metabolism and basolateral glucose. Many of these changes were also observed in hpBMEC, indicating that these changes were not specific to hiBMEC. Finally, we found that HPβCD co-treatment partially hiBMEC restored metabolic phenotype. Our work reveals for the first time that NPC1 inhibition may alter BMEC metabolism, and that these metabolic changes can be partially corrected with HPβCD. This evidence positions the brain vasculature as a potential contributor to neurodegeneration in NP-C and highlights the need for further studies to determine whether metabolic correction of brain endothelium could be a feasible strategy to delay or even treat disease manifestations.

NPC1 inhibition increased hiBMEC glycolytic flux, which aligns with reports of increased glycolysis following NPC1 inhibition in other cell types and animal models (Charman et al., 2010; Kennedy et al., 2014). Metabolomic analysis of NPC1-null mice cerebellar tissue at presymptomatic (3 weeks old), early symptomatic (5 weeks old), and late stage (7 weeks old) disease phases showed elevated lactate (Kennedy et al., 2013). Microglia from NPC1-KO mice also show an increasingly glycolytic phenotype, as evidenced by increased ECAR and expression of glycolytic genes such as glyceraldehyde-3-phosphate dehydrogenase (*GAPDH*) (Cougnoux et al., 2018). Similarly, NPC1 inhibition in CHO cells increased lactate secretion (Kennedy et al., 2014). We also found increased glucose flux into glycolysis side branch pathways such as the PPP and HBP in U18666A-treated hiBMEC, which aligns with a previous report of PPP gene upregulation in NPC1-null mice microglia (Cougnoux et al., 2018).

Increased glycolytic and PPP flux may occur for several reasons in NPC1-deficient cells. NPC1 deficiency increases expression of cholesterol biosynthetic enzymes, including *HMGCR*, *SREBF1*, and *SREBF2*. Increased *SREBF1* then increases expression of glycolytic genes such as *HK2* and may therefore directly upregulate glycolysis (Gosmain et al., 2005; Horton et al., 2002). However, when we co-treated U18-treated BMECs with the SREBP inhibitor betulin (Tang et al., 2011) and anti-

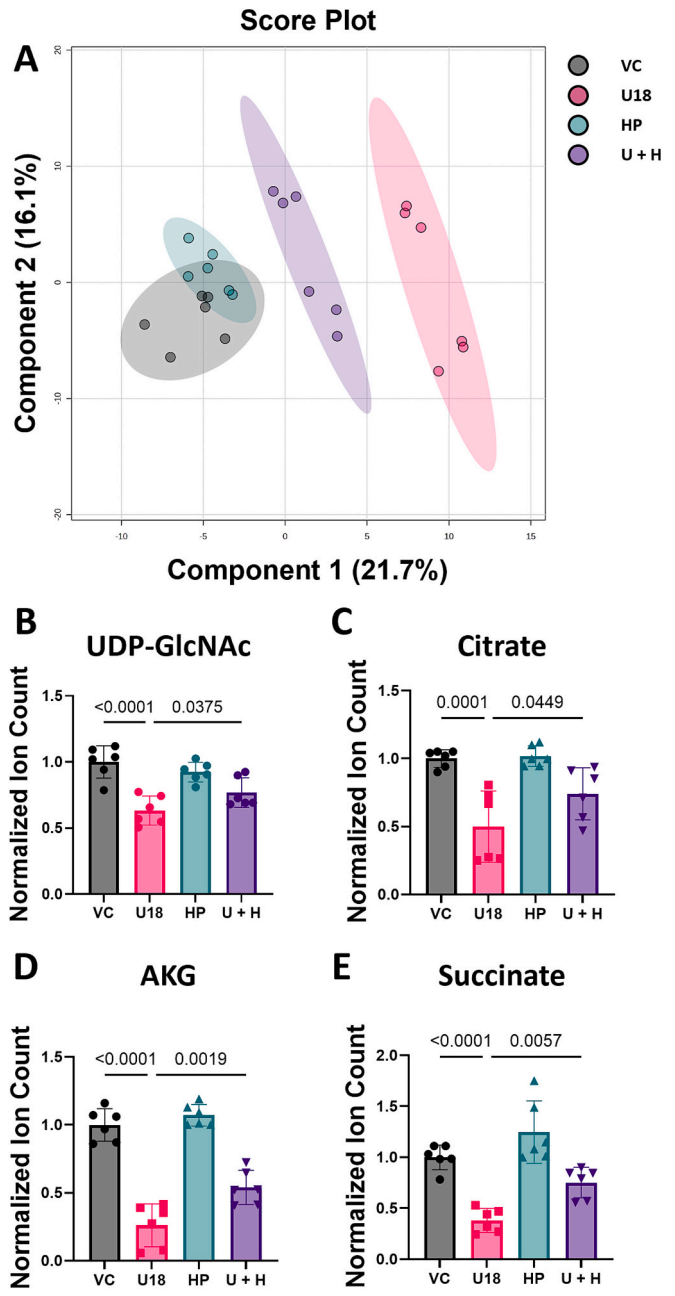

Fig. 8. HPβCD partially restored intracellular metabolites in U18666A-treated hiBMEC. (A) PCA score plot of total ion abundance, measured by LC-MS. Normalized ion count for (B) UDP-GlcNAc, (C) citrate (D) α-ketoglutarate (AKG) and (E) succinate ($n = 6$ samples). All data shown as mean +/− standard deviation. Each data point was normalized to the mean of the VC group for each experiment. One-way ANOVA followed by Sidak's Multiple Comparisons Test used to compare multiple groups.

SREBP1/2 siRNA, we did not observe a decrease in glycolysis (data not shown). Additionally, cholesterol is an energetically expensive molecule to synthesize, requiring several moles of ATP, NADPH, and acetyl-CoA. The PPP is the primary driver of NADPH production. Studies in cancer cells show that increased cholesterol biosynthesis depletes NAPDH, which then increases PPP flux (Hu et al., 2023). The PPP may also be upregulated to combat oxidative stress, which is elevated in NPC1-deficient mouse brain tissue (Kennedy et al., 2013), CHO cells (Kennedy et al., 2014), patient-derived neurons (Jürs et al., 2020), and mouse microglia (Cougnoux et al., 2018). Oxidative stress reduces NADPH levels (Moon et al., 2020), which can increase compensatory PPP flux and subsequentially increase glycolysis to fuel the PPP. Increased glycolysis could alternatively be triggered as cells compensate for ATP loss due to diminished mitochondrial metabolism.

Increased BMEC glycolysis could have important implications for NP-C disease progression. NPC-1 inhibition decreased glucose availability on the basolateral side of the brain endothelium. Interestingly, cerebral glucose hypometabolism was recently observed in NP-C patients, predominantly in the posterior cingulate gyrus, and correlated with clinical severity (Kao et al., 2021; Lau et al., 2021). Glucose hypometabolism is typically associated with dysfunctional BMEC glucose transport due to decreased glucose transporter levels and function (Daulatzai, 2017; Winkler et al., 2015). While BMEC take up more glucose with NPC inhibition, they also consume more glucose for their own metabolic needs, which could lead to decreased glucose for other brain cells. Further investigation is needed to delineate whether this is a causal factor in glucose hypometabolism in NP-C patients. Glucose hypometabolism often precedes cognitive decline in other neurodegenerative diseases such as AD, suggesting that BMEC glucose metabolism has potential as a therapeutic target (Daulatzai, 2017).

We also observed increased lactate secretion into the basolateral compartment of both U18666A-treated and NPC1-KO hiBMEC. This could indicate a compensatory metabolic adaption that allows endothelial cells to use glucose for their own anaerobic metabolism and still provide energy for other brain cells (e.g., pericytes, neurons) through lactate (Lee et al., 2022; Riske et al., 2017). However, brain lactate is an excitatory molecule that can induce neurotoxic effects. Brain lactate concentration is typically between 0.5 and 2 mmol/L, with it reaching the higher levels during exercise (Xue et al., 2022). Notably, our studies showed that 48 h of U18666A treatment resulted in lactate levels that exceeded this upper limit. Cerebral lactate is also elevated in several neurodegenerative diseases, including multiple sclerosis, AD, and amyotrophic lateral sclerosis. Primary neurons exposed to high lactate concentrations show increased excitotoxicity, cytosolic reactive oxygen species (ROS), and endoplasmic reticular stress markers (Chapp et al., 2021). Further investigation is therefore needed whether lactate levels are elevated to toxic levels in NP-C and whether BMECs significantly contribute to its accumulation.

Our work also demonstrates altered mitochondrial metabolism in NPC-1 deficient BMEC. Although endothelial cells are highly glycolytic and generate most of their ATP from glycolysis (Li et al., 2019), changes in mitochondrial function can still be devastating due to the role of endothelial mitochondria in signaling, angiogenesis, autophagy, and redox balance (Kluge et al., 2013). Dysfunctional mitochondria have been implicated in vascular pathologies such as atherosclerosis, particularly due to their role in increasing reactive oxygen species (Ciccarelli et al., 2023). The change in mitochondrial respiration capacity, defined as the mitochondrial capacity to meet emergent energetic needs during acute stress or large energetic loads (Marchetti et al., 2020), was particularly dramatic. Notably, spare respiratory capacity is important in responding to oxidative stress in endothelial cells, and decreased capacity may make endothelial more vulnerable to oxidative stress (Dranka et al., 2010).

Several factors could lead to the decreased mitochondrial respiration and membrane potential observed in U18666A-treated BMEC. Reduced TCA metabolite labeling indicates decreased influx of glucose-derived pyruvate into the mitochondria, increased influx of tertiary and anaplerotic sources to fuel the TCA cycle, or a combination of both. INST-MFA suggests a significant decrease in carbon supply is at fault, as pyruvate transport to the mitochondria decreased by 46 % while α-ketoglutarate and citrate are both transported out of the mitochondria. Our data agree with studies in NPC1-null mice that showed decreased cerebral acetyl-CoA, which in brain tissue is primarily sourced by pyruvate decarboxylation in the mitochondria. In 5-week-old mice, gene expression of *PDH* (which catalyzes mitochondrial decarboxylation of pyruvate into acetyl-CoA) decreased, while *PFK1*, *LDHA, PDH* kinase (which inhibits PDH) and pyruvate carboxylase (*PC*, which converts pyruvate to

oxaloacetate in the mitochondria) increased. Two forms of malic enzyme (which shuttles malate from the mitochondria for conversion into pyruvate) also decreased in 3-week-old mice (Kennedy et al., 2013). To test if decreased mitochondrial flux was caused by PDH inhibition in our cells, we treated U18666A-treated hiBMEC with dichloroacetate (DCA), a PDH activator. However, we did not observe significant changes in OCR with PDH co-treatment (data not shown). This aligns with a previous study in NPC1-deficient CHO cells, in which minimal mitochondrial restoration was observed with DCA treatment (Kennedy et al., 2014).

In NPC1-deficient CHO cells, mitochondrial function was restored by inhibiting endosomal metastatic lymph node protein 64 (MLN64), which shuttles endosomal cholesterol to the mitochondria (Charman et al., 2010). MLN64 expression was elevated in *Npc1*-null mice liver tissue and NPC1-deficient CHO cells. Treatment of NPC1-deficient CHO cells with MLN64-siRNA reduced mitochondrial cholesterol and restored mitochondrial membrane potential and superoxide levels (Balboa et al., 2017; Charman et al., 2010). We were unable to isolate pure mitochondria to measure mitochondrial cholesterol in U18666A-treated hiBMEC. However, LC-MS showed high pregnenolone in U18666A-treated hiBMEC. Pregnenolone is synthesized from cholesterol that accumulates in the mitochondria; therefore, increased pregnenolone in U18666A-treated cells suggests cholesterol accumulation in the mitochondria.

We also observed significant differences in both intracellular and extracellular acyl-carnitines. Carnitines play essential roles in fatty acid metabolism, which is upregulated in quiescent endothelial cells (Kalucka et al., 2018). Specifically, carnitines are formed when acyl-CoAs derived from fatty acids are bound to free carnitine to import them into the mitochondria. Disruption of quiescence may in turn disrupt fatty acid oxidation and subsequently carnitine metabolism. Carnitines are also synthesized from lysine and methionine; however, we did not observe any significant differences in these amino acids in U18666A-treated hiBMEC. High levels of acyl carnitines are typically associated with mitochondrial dysfunction while deficiencies are not as well characterized (Flanagan et al., 2010). A similar metabolic phenotype was previously observed in pulmonary microvascular endothelial cells with mutations in bone morphogenetic protein receptor 2 (BMPR2) (Fessel et al., 2012). These cells also showed an increase in glycolysis, decrease in carnitines, and decrease in TCA cycle intermediates (Fessel et al., 2012). Loss of BMPR2 has been shown to lead to mitochondrial dysfunction (Diebold et al., 2015). Interestingly, NPC1 is essential for BMPR2-mediated insulin signaling, acting as a scaffold to recruit BMPR2 to insulin receptor (Mao et al., 2021). It is therefore plausible that disruption of this scaffolding interaction may perturb mitochondrial and carnitine metabolism in BMEC through a BMPR2-mediated mechanism.

Little is currently known regarding the relationship between cholesterol trafficking or metabolism and the HBP. However, a common link between UDP-GlcNAc and cholesterol synthesis is their dependency on acetyl-CoA, which is an essential substrate for both pathways. Decreased UDP-GlcNAc may occur due to competition with lipid and cholesterol biosynthetic factors for acetyl-CoA following U18666A treatment. GFAT1, the rate-limiting HBP enzyme that metabolizes F6P into glucosamine-6-phosphate, is inhibited by UDP-GlcNAc and G6P (Paneque et al., 2023). Although we did not observe increased GFAT protein levels, decreased HBP by-products may lead to increased GFAT1 activity in U18666A-treated hiBMEC (Lockridge and Hanover, 2022). Decreased UDP-GLcNAc may also occur due to increased degradation of UDP-GlcNAc. This could also result in increased HBP activity as a compensatory mechanism to restore UDP-GlcNAc levels.

Metabolic changes in glycolysis, HBP, and mitochondria incurred by NPC1 inhibition were consistent between hpBMEC and hiBMEC. However, glucose flux into the PPP and glycogen synthesis were opposite in hiBMEC and hpBMEC. We recently showed that while hpBMECs are similar to hiBMECs in glucose metabolism (Weber et al., 2024), there are significant differences in mitochondrial morphology and metabolic pathways, particularly glutamate metabolism (Weber et al., 2024). hpBMECs may have a higher capacity to increase NAPDH through other mitochondrial-based pathways, such as malic enzyme or isocitrate dehydrogenase, that lower or prevent their dependence on the PPP and glycolysis. These differences may also allow hpBMEC to minimize changes to glycolysis following U18666A treatment.

HPβCD partially rescued the hiBMEC intracellular metabolome following U18666A treatment, including OCR, TCA metabolites, and carnitine. Interestingly, HPβCD also reduced pregnenolone, an indicator of mitochondrial cholesterol accumulation, but did not restore *SREBF2* or *HMGCR* mRNA levels. Together, these data suggest that mitochondrial cholesterol and pregnenolone accumulation are only partially responsible for the dysfunctional metabolic phenotype in U18666A-treated hiBMEC. Full phenotype restoration may require effective targeting of cholesterol biosynthetic factors as well. Furthermore, it suggests that HPβCD, which has poor blood-brain barrier permeability, could exert therapeutic or neuroprotective effects without penetrating the blood-brain barrier by restoring metabolic phenotype in brain endothelium.

Although this study provides new insights into how NPC-1 inhibition alters metabolism in BMEC, it has several limitations. First, BMEC are closely integrated in the neurovascular unit, where they dynamically interact with and respond to cues from other brain cells. In our study, in vitro models were simplified to focus on only one cell type. Second, we performed several experiments on BMEC cultured on impermeable well plates instead of permeable Transwell inserts, which are not as relevant in replicating barrier physiology. Third, the labeling schemes used were not comprehensive as we only used glucose labels. Glutamine labels may be more informative to analyze flux in the TCA cycle. For comprehensive metabolic flux analysis, we would need to use a parallel labeling scheme to target glycolysis and the TCA cycle (Crown et al., 2016; Woo Suk and Antoniewicz, 2013). Experimental constraints further prevented us from measuring isotopomers of cholesterol and its precursors. We were also unable to robustly quantify fatty acid isotopomers. The INST-MFA network model therefore did not include fatty acid or cholesterol synthesis and prevented us from quantifying flux in these pathways. This led to some unrealistic assumptions in the model, such as that all cytosolic acetyl-CoA can only be used to generate UDP-GlcNAc, and prevented modeling of acetyl-CoA flux into other intracellular sinks.

5. Conclusions

NPC1 inhibition in BMEC via U18666A treatment significantly perturbed metabolism by increasing glycolysis and decreasing mitochondrial oxidative respiration. BMEC also changed intracellular acyl carnitine and TCA metabolite levels in response to NPC1 inhibition. These changes were partially attenuated by HPβCD. Together, our results show a potential role for BMEC metabolism in NP-C pathogenesis, as altered BMEC metabolism may lead to vascular dysfunction, decreased brain glucose, and altered cerebral metabolic environment.

Supplementary data to this article can be found online at https://doi.org/10.1016/j.nbd.2024.106769.

Funding

The authors gratefully acknowledge funding support from the Brain and Behavior Institute at the University of Maryland through the BBI Seed Grant Program to AMC and GS, the National Science Foundation (CBET 2211966) to AMC and GS, the National Institutes of Health (No. R01HL165193) to AMC and GS, and the National Institutes of Health (No. R01HL140239-01) to AMC, the NSF DGE-1632976 to BM, the National Niemann-Pick Disease Foundation to BM, the AHA predoctoral fellowship to BM, the National Science Foundation Graduate Research Fellowship Program (DGE 1840340) to CMW, the Fischell Fellowship in Biomedical Engineering through the Fischell Institute to CMW, and the University of Maryland ASPIRE Program to VA.

CRediT authorship contribution statement

Bilal Moiz: Writing – review & editing, Writing – original draft, Visualization, Validation, Methodology, Investigation, Funding acquisition, Formal analysis, Data curation, Conceptualization. **Matthew Walls:** Visualization, Investigation, Data curation. **Viviana Alpizar Vargas:** Visualization, Validation, Investigation, Data curation. **Anirudh Addepalli:** Validation, Investigation, Data curation. **Callie Weber:** Writing – review & editing, Validation, Data curation. **Andrew Li:** Validation, Investigation, Data curation. **Ganesh Sriram:** Writing – review & editing, Supervision, Methodology, Funding acquisition, Formal analysis, Conceptualization. **Alisa Morss Clyne:** Writing – review & editing, Writing – original draft, Visualization, Supervision, Resources, Project administration, Methodology, Funding acquisition, Conceptualization.

Declaration of competing interest

The authors declare the following financial interests/personal relationships which may be considered as potential competing interests:

Alisa Clyne reports financial support was provided by National Institutes of Health. Alisa Clyne reports financial support was provided by National Science Foundation. Bilal Moiz reports financial support was provided by National Niemann Pick Disease Foundation. Bilal Moiz reports financial support was provided by National Science Foundation. Callie Weber reports financial support was provided by National Science Foundation. Bilal Moiz reports financial support was provided by American Heart Association. If there are other authors, they declare that they have no known competing financial interests or personal relationships that could have appeared to influence the work reported in this paper.

Acknowledgements

The authors would like to thank Forbes Porter, Christopher Wassif, and Marzyeh Kheradmand for their valuable contributions to this research, as well as the University of Colorado School of Medicine Metabolomics Core for mass spectrometry analysis.

Data availability

Computational and mass spectrometry data will be made available. All other data can be provided upon request.

References

Abi-Mosleh, L., Infante, R.E., Radhakrishnan, A., Goldstein, J.L., Brown, M.S., 2009. Cyclodextrin overcomes deficient lysosome-to-endoplasmic reticulum transport of cholesterol in Niemann-pick type C cells. Proc. Natl. Acad. Sci. USA 106, 19316–19321. https://doi.org/10.1073/PNAS.0910916106.

Antoniewicz, M.R., 2018. A guide to (13)C metabolic flux analysis for the cancer biologist. Exp. Mol. Med. 50, 19. https://doi.org/10.1038/s12276-018-0060-y.

Balboa, E., Castro, J., Pinochet, M.J., Cancino, G.I., Matías, N., José Sáez, P., Martínez, A., Álvarez, A.R., Garcia-Ruiz, C., Fernandez-Checa, J.C., Zanlungo, S., 2017. MLN64 induces mitochondrial dysfunction associated with increased mitochondrial cholesterol content. Redox Biol. 12, 274–284. https://doi.org/10.1016/J.REDOX.2017.02.024.

Beltroy, E.P., Richardson, J.A., Horton, J.D., Turley, S.D., Dietschy, J.M., 2005. Cholesterol accumulation and liver cell death in mice with Niemann-pick type C disease. Hepatology 42, 886–893. https://doi.org/10.1002/hep.20868.

Beyß, M., Parra-Peña, V.D., Ramirez-Malule, H., Nöh, K., 2021. Robustifying experimental tracer design for13C-metabolic flux analysis. Front. Bioeng. Biotechnol. 9. https://doi.org/10.3389/FBIOE.2021.685323/FULL.

Cenedella, R.J., 2009. Cholesterol synthesis inhibitor U18666A and the role of sterol metabolism and trafficking in numerous pathophysiological processes. Lipids 44, 477–487. https://doi.org/10.1007/s11745-009-3305-7.

Chapp, A.D., Behnke, J.E., Driscoll, K.M., Hahka, T., LaLonde, Z., Shan, Z., Chen, Q.H., 2021. Elevated L-lactate promotes major cellular pathologies associated with neurodegenerative diseases. Neurosci. Bull. 37, 380. https://doi.org/10.1007/S12264-020-00611-6.

Charman, M., Kennedy, B.E., Osborne, N., Karten, B., 2010. MLN64 mediates egress of cholesterol from endosomes to mitochondria in the absence of functional Niemann-pick type C1 protein. J. Lipid Res. 51, 1023–1034. https://doi.org/10.1194/JLR.M002345.

Chernoff, H., Lehmann, E.L., 2012. The use of maximum likelihood estimates in $\chi 2$ tests for goodness-of-fit. In: Rojo, J. (Ed.), Selected Works of E. L. Lehmann. Springer US, Boston, MA, pp. 541–549. https://doi.org/10.1007/978-1-4614-1412-4_47.

Ciccarelli, G., Conte, S., Cimmino, G., Maiorano, P., Morrione, A., Giordano, A., 2023. Mitochondrial dysfunction: the hidden player in the pathogenesis of atherosclerosis? Int. J. Mol. Sci. https://doi.org/10.3390/ijms24021086.

Clasquin, M.F., Melamud, E., Rabinowitz, J.D., 2012. LC-MS data processing with MAVEN: a Metabolomic analysis and visualization engine. Curr. Protoc. Bioinformatics. https://doi.org/10.1002/0471250953.bi1411s37.

Cougnoux, A., Drummond, R.A., Collar, A.L., Iben, J.R., Salman, A., Westgarth, H., Wassif, C.A., Cawley, N.X., Farhat, N.Y., Ozato, K., Lionakis, M.S., Porter, F.D., 2018. Microglia activation in Niemann-pick disease, type C1 is amendable to therapeutic intervention. Hum. Mol. Genet. 27, 2076–2089. https://doi.org/10.1093/hmg/ddy112.

Crown, S.B., Long, C.P., Antoniewicz, M.R., 2016. Optimal tracers for parallel labeling experiments and (13)C metabolic flux analysis: a new precision and synergy scoring system. Metab. Eng. 38, 10–18. https://doi.org/10.1016/j.ymben.2016.06.001.

Daulatzai, M.A., 2017. Cerebral hypoperfusion and glucose hypometabolism: key pathophysiological modulators promote neurodegeneration, cognitive impairment, and Alzheimer's disease. J. Neurosci. Res. 95, 943–972. https://doi.org/10.1002/jnr.23777.

Diebold, I., Hennigs, J.K., Feldman, B.J., Correspondence, M.R., 2015. BMPR2 preserves mitochondrial function and DNA during Reoxygenation to promote endothelial cell survival and reverse pulmonary hypertension. Cell Metab. 21, 596–608. https://doi.org/10.1016/j.cmet.2015.03.010.

Dranka, B.P., Hill, B.G., Darley-Usmar, V.M., 2010. Mitochondrial reserve capacity in endothelial cells: the impact of nitric oxide and reactive oxygen species. Free Radic. Biol. Med. 48, 905. https://doi.org/10.1016/J.FREERADBIOMED.2010.01.015.

Fessel, J.P., Hamid, R., Wittmann, B.M., Robinson, L.J., Blackwell, T., Tada, Y., Tanabe, N., Tatsumi, K., Hemnes, A.R., West, J.D., 2012. Metabolomic analysis of bone morphogenetic protein receptor type 2 mutations in human pulmonary endothelium reveals widespread metabolic reprogramming. Pulm. Circ. 2, 201–213. https://doi.org/10.4103/2045-8932.97606/ASSET/IMAGES/LARGE/10.4103_2045-8932.97606-FIG 7.JPEG.

Flanagan, J.L., Simmons, P.A., Vehige, J., Willcox, M.D.P., Garrett, Q., 2010. Role of carnitine in disease. Nutr. Metab. (Lond.) 7, 30. https://doi.org/10.1186/1743-7075-7-30.

Goldstein, G.W., Csjtey, J., Diamond, I., 1977. Carrier mediated glucose transport in capillaries isolated from rat brain1. J. Neurochem. 28, 725–728. https://doi.org/10.1111/J.1471-4159.1977.TB10619.X.

Gosmain, Y., Dif, N., Berbe, Vanessa, Loizon, Emmanuelle, Rieusset, Jennifer, Vidal, Hubert, Lefai, Etienne, Berbe, V., Loizon, E., Rieusset, J., Vidal, H., Lefai, E., 2005. Regulation of SREBP-1 expression and transcriptional action on HKII and FAS genes during fasting and refeeding in rat tissues. J. Lipid Res. 46. https://doi.org/10.1194/jlr.M400261-JLR200.

Greene, C., Hanley, N., Reschke, C.R., Reddy, A., Mäe, M.A., Connolly, R., Behan, C., O'Keeffe, E., Bolger, I., Hudson, N., Delaney, C., Farrell, M.A., O'Brien, D.F., Cryan, J., Brett, F.M., Beausang, A., Betsholtz, C., Henshall, D.C., Doherty, C.P., Campbell, M., 2022. Microvascular stabilization via blood-brain barrier regulation prevents seizure activity. Nat. Commun. 13 (1), 1–13. https://doi.org/10.1038/s41467-022-29657-y.

Hammond, N., Munkacsi, A.B., Sturley, S.L., 2019. The complexity of a monogenic neurodegenerative disease: more than two decades of therapeutic driven research into Niemann-pick type C disease. Biochim. Biophys. Acta (BBA) Mol. Cell Biol. Lipids 1864, 1109–1123. https://doi.org/10.1016/j.bbalip.2019.04.002.

Horton, J.D., Goldstein, J.L., Brown, M.S., 2002. SREBPs: activators of the complete program of cholesterol and fatty acid synthesis in the liver. J. Clin. Invest. 109, 1125–1131. https://doi.org/10.1172/jci15593.

Hu, J., Liu, N., Song, D., Steer, C.J., Zheng, G., Song, G., 2023. A positive feedback between cholesterol synthesis and the pentose phosphate pathway rather than glycolysis promotes hepatocellular carcinoma. Oncogene 42 (39), 2892–2904. https://doi.org/10.1038/s41388-023-02757-9.

Jang, C., Chen, L., Rabinowitz, J.D., 2018. Metabolomics and isotope tracing. Cell 173, 822–837. https://doi.org/10.1016/J.CELL.2018.03.055.

Jia, Z., Yang, M., Zhao, Y., Li, X., Yang, C., Qiao, L., Li, H., Du, J., Lin, J., Guan, L., 2023. CRISPR-Cas9-mediated NPC1 gene deletion enhances HEK 293 T cell adhesion by regulating E-cadherin. Mol. Biotechnol. 65, 252–262. https://doi.org/10.1007/s12033-022-00503-2.

Jiang, L., Boufersaoui, A., Yang, C., Ko, B., Rakheja, D., Guevara, G., Hu, Z., DeBerardinis, R.J., 2017. Quantitative metabolic flux analysis reveals an unconventional pathway of fatty acid synthesis in cancer cells deficient for the mitochondrial citrate transport protein. Metab. Eng. 43, 198–207. https://doi.org/10.1016/j.ymben.2016.11.004.

Jürs, A.V., Völkner, C., Liedtke, M., Huth, K., Lukas, J., Hermann, A., Frech, M.J., 2020. Oxidative stress and alterations in the Antioxidative defense system in neuronal cells derived from NPC1 patient-specific induced pluripotent stem cells. Int. J. Mol. Sci. 21, 7667. https://doi.org/10.3390/IJMS21207667.

Kalucka, J., Bierhansl, L., Conchinha, N.V., Missiaen, R., Elia, I., Brüning, U., Scheinok, S., Treps, L., Cantelmo, A.R., Dubois, C., de Zeeuw, P., Goveia, J., Zecchin, A., Taverna, F., Morales-Rodriguez, F., Brajic, A., Conradi, L.C., Schoors, S., Harjes, U., Vriens, K., Pilz, G.A., Chen, R., Cubbon, R., Thienpont, B., Cruys, B., Wong, B.W., Ghesquière, B., Dewerchin, M., De Bock, K., Sagaert, X., Jessberger, S., Jones, E.A.V., Gallez, B., Lambrechts, D., Mazzone, M., Eelen, G., Li, X., Fendt, S.M., Carmeliet, P., 2018. Quiescent endothelial cells upregulate fatty acid β-oxidation for

Vasculoprotection via redox homeostasis. Cell Metab. 28, 881–894 e13. https://doi.org/10.1016/j.cmet.2018.07.016.
Kao, Y.H., Cheng, M., Velakoulis, D., Walterfang, M., Sivaratnam, D., 2021. Brain hypometabolism in rare genetic neurodegenerative disease: Niemann-pick disease type C, spinocerebellar ataxia and Huntington disease assessed by FDG PET. Asia Ocean J. Nucl. Med. Biol. 9, 167–172. https://doi.org/10.22038/aojnmb.2020.52511.1362.
Kennedy, B.E., LeBlanc, V.G., Mailman, T.M., Fice, D., Burton, I., Karakach, T.K., Karten, B., 2013. Pre-symptomatic activation of antioxidant responses and alterations in glucose and pyruvate metabolism in Niemann-pick type C1-deficient murine brain. PLoS One 8, e82685.
Kennedy, B.E., Madreiter, C.T., Vishnu, N., Malli, R., Graier, W.F., Karten, B., 2014. Adaptations of energy metabolism associated with increased levels of mitochondrial cholesterol in Niemann-pick type C1-deficient cells. J. Biol. Chem. 289, 16278. https://doi.org/10.1074/JBC.M114.559914.
Kluge, M.A., Fetterman, J.L., Vita, J.A., 2013. Mitochondria and endothelial function. Circ. Res. 112, 1171–1188. https://doi.org/10.1161/CIRCRESAHA.111.300233.
Kresojević, N., Dobričić, V., Svetel, M., Kostić, V., 2014. Mutations in Niemann pick type C gene are risk factor for Alzheimer's disease. Med. Hypotheses 83, 559–562. https://doi.org/10.1016/j.mehy.2014.08.025.
Kyrtata, N., Emsley, H.C.A., Sparasci, O., Parkes, L.M., Dickie, B.R., 2021. A systematic review of glucose transport alterations in Alzheimer's disease. Front. Neurosci. https://doi.org/10.3389/fnins.2021.626636.
Lamri, A., Pigeyre, M., Garver, W.S., Meyre, D., 2018. The extending Spectrum of NPC1-related human disorders: from Niemann-pick C1 disease to obesity. Endocr. Rev. 39, 192–220. https://doi.org/10.1210/er.2017-00176.
Lau, T.Y., Kao, Y.H., Toh, H.B., Sivaratnam, D., Lichtenstein, M., Velakoulis, D., Walterfang, M., 2021. Brain hypometabolic changes in 14 adolescent-adult patients with Niemann-pick disease type C assessed by 18F-fluorodeoxyglucose positron emission tomography. J. Neurol. 268, 3878–3885. https://doi.org/10.1007/s00415-021-10535-4.
Lee, H., Xu, Y., Zhu, X., Jang, C., Choi, W., Bae, H., Wang, W., He, L., Jin, S., Arany, Z., Simons, M., 2022. Endothelium-derived lactate is required for pericyte function and blood–brain barrier maintenance. EMBO J. 41. https://doi.org/10.15252/embj.2021109890.
Li, X., Sun, X., Carmeliet, P., 2019. Hallmarks of endothelial cell metabolism in health and disease. Cell Metab. https://doi.org/10.1016/j.cmet.2019.08.011.
Liu, B., Turley, S.D., Burns, D.K., Miller, A.M., Repa, J.J., Dietschy, J.M., 2009. Reversal of defective lysosomal transport in NPC disease ameliorates liver dysfunction and neurodegeneration in the npc1−/− mouse. Proc. Natl. Acad. Sci. USA 106, 2377–2382. https://doi.org/10.1073/PNAS.0810895106.
Lockridge, A., Hanover, J.A., 2022. A nexus of lipid and O-Glcnac metabolism in physiology and disease. Front. Endocrinol. (Lausanne) 13. https://doi.org/10.3389/FENDO.2022.943576/FULL.
Mao, H., Li, L., Fan, Q., Angelini, A., Saha, P.K., Wu, H., Ballantyne, C.M., Hartig, S.M., Xie, L., Pi, X., 2021. Loss of bone morphogenetic protein-binding endothelial regulator causes insulin resistance. Nat. Commun. 12. https://doi.org/10.1038/s41467-021-22130-2.
Marchetti, P., Fovez, Q., Germain, N., Khamari, R., Kluza, J., 2020. Mitochondrial spare respiratory capacity: mechanisms, regulation, and significance in non-transformed and cancer cells. FASEB J. 34, 13106–13124. https://doi.org/10.1096/FJ.202000767R.
Melamud, E., Vastag, L., Rabinowitz, J.D., 2010. Metabolomic analysis and visualization engine for LC-MS data HHS public access. Anal. Chem. 82, 9818–9826. https://doi.org/10.1021/ac1021166.
Mergenthaler, P., Lindauer, U., Dienel, G.A., Meisel, A., 2013. Sugar for the brain: the role of glucose in physiological and pathological brain function. Trends Neurosci. https://doi.org/10.1016/j.tins.2013.07.001.
Millard, P., Delépine, B., Guionnet, M., Heuillet, M., Bellvert, F., Létisse, F., 2019. IsoCor: isotope correction for high-resolution MS labeling experiments. Bioinformatics 35, 4484–4487. https://doi.org/10.1093/bioinformatics/btz209.
Moiz, B., Garcia, J., Basehore, S., Sun, A., Li, A., Padmanabhan, S., Albus, K., Jang, C., Sriram, G., Clyne, A.M., 2021. 13 C metabolic flux analysis indicates endothelial cells attenuate metabolic perturbations by modulating TCA activity. Metabolites 11. https://doi.org/10.3390/METABO11040226.
Moiz, B., Li, A., Padmanabhan, S., Sriram, G., Clyne, A.M., 2022. Isotope-assisted metabolic flux analysis: a powerful technique to gain new insights into the human metabolome in health and disease. Metabolites 12, 1066. https://doi.org/10.3390/METABO12111066.
Moon, S.J., Dong, W., Stephanopoulos, G.N., Sikes, H.D., 2020. Oxidative pentose phosphate pathway and glucose anaplerosis support maintenance of mitochondrial NADPH pool under mitochondrial oxidative stress. Bioeng. Transl. Med 5. https://doi.org/10.1002/BTM2.10184.
Mosconi, L., Pupi, A., De Leon, M.J., 2008. Brain glucose hypometabolism and oxidative stress in preclinical Alzheimer's disease. In: Annals of the new York Academy of Sciences. Blackwell Publishing Inc., pp. 180–195. https://doi.org/10.1196/annals.1427.007
Neal, E.H., Marinelli, N.A., Shi, Y., McClatchey, P.M., Balotin, K.M., Gullett, D.R., Hagerla, K.A., Bowman, A.B., Ess, K.C., Wikswo, J.P., Lippmann, E.S., 2019. A Simplified, Fully Defined Differentiation Scheme for Producing Blood-Brain Barrier Endothelial Cells from Human iPSCs. Stem cell reports 12 (6), 1380–1388. https://doi.org/10.1016/j.stemcr.2019.05.008. PMID: 31189096; PMCID: PMC6565873.
Nelson, A.R., Sweeney, M.D., Sagare, A.P., Zlokovic, B.V., 2016. Neurovascular dysfunction and neurodegeneration in dementia and Alzheimer's disease. Biochim. Biophys. Acta 1862, 887–900. https://doi.org/10.1016/J.BBADIS.2015.12.016.
Nemkov, T., D'Alessandro, A., Hansen, K.C., 2015. Three-minute method for amino acid analysis by UHPLC and high-resolution quadrupole orbitrap mass spectrometry. Amino Acids 47, 2345–2357. https://doi.org/10.1007/s00726-015-2019-9.
Nemkov, T., Hansen, K.C., D'Alessandro, A., 2017. A three-minute method for high-throughput quantitative metabolomics and quantitative tracing experiments of central carbon and nitrogen pathways. Rapid Commun. Mass Spectrom. 31, 663–673. https://doi.org/10.1002/rcm.7834.
Nemkov, T., Reisz, J.A., Gehrke, S., Hansen, K.C., D'Alessandro, A., 2019. High-Throughput Metabolomics: Isocratic and Gradient Mass Spectrometry-Based Methods, pp. 13–26. https://doi.org/10.1007/978-1-4939-9236-2_2.
Noguchi, S., Ishikawa, H., Wakita, K., Matsuda, F., Shimizu, H., 2020. Direct and quantitative analysis of altered metabolic flux distributions and cellular ATP production pathway in fumarate hydratase-diminished cells. Sci. Rep. 10. https://doi.org/10.1038/s41598-020-70000-6.
Paneque, A., Fortus, H., Zheng, J., Werlen, G., Jacinto, E., 2023. The Hexosamine biosynthesis pathway: regulation and function. Genes (Basel) 14. https://doi.org/10.3390/GENES14040933.
Pang, Z., Zhou, G., Ewald, J., Chang, L., Hacariz, O., Basu, N., Xia, J., 2022. Using MetaboAnalyst 5.0 for LC–HRMS spectra processing, multi-omics integration and covariate adjustment of global metabolomics data. Nat. Protoc. 17, 1735–1761. https://doi.org/10.1038/s41596-022-00710-w.
Rahim, M., Ragavan, M., Deja, S., Merritt, M.E., Burgess, S.C., Young, J.D., 2022. INCA 2.0: A tool for integrated, dynamic modeling of NMR- and MS-based isotopomer measurements and rigorous metabolic flux analysis. Metabolic engineering 69, 275–285. https://doi.org/10.1016/j.ymben.2021.12.009. PMID: 34965470; PMCID: PMC8789327.
Raut, S., Patel, R., Pervaiz, I., Al-Ahmad, A.J., 2022. Abeta peptides disrupt the barrier integrity and glucose metabolism of human induced pluripotent stem cell-derived brain microvascular endothelial cells. Neurotoxicology 89, 110–120. https://doi.org/10.1016/J.NEURO.2022.01.007.
Reisz, J.A., Zheng, C., D'Alessandro, A., Nemkov, T., 2019. Untargeted and semi-targeted lipid analysis of biological samples using mass spectrometry-based metabolomics. In: D'Alessandro, A. (Ed.), High-Throughput Metabolomics: Methods and Protocols. Springer, New York, New York, NY, pp. 121–135. https://doi.org/10.1007/978-1-4939-9236-2_8.
Riske, L., Thomas, R.K., Baker, G.B., Dursun, S.M., 2017. Lactate in the brain: an update on its relevance to brain energy, neurons, glia and panic disorder. Ther. Adv. Psychopharmacol. 7, 85. https://doi.org/10.1177/2045125316675579.
Sharma, R., Hastings, C., Staretz-Chacham, O., Raiman, J., Paucar, M., Spiegel, R., Murray, B., Hurst, B., Liu, B., Kjems, L., Hrynkow, S., 2023. Long-term administration of intravenous Trappsol® Cyclo™ (HP-β-CD) results in clinical benefits and stabilization or slowing of disease progression in patients with Niemann-pick disease type C1: results of an international 48-week phase I/II trial. Mol. Genet. Metab. Rep. 36. https://doi.org/10.1016/J.YMGMR.2023.100988.
Tang, J.J., Li, J.G., Qi, W., Qiu, W.W., Li, P.S., Li, B.L., Song, B.L., 2011. Inhibition of SREBP by a small molecule, betulin, improves hyperlipidemia and insulin resistance and reduces atherosclerotic plaques. Cell Metab. 13, 44–56. https://doi.org/10.1016/J.CMET.2010.12.004.
Tiscione, S.A., Casas, M., Horvath, J.D., Lam, V., Hino, K., Ory, D.S., Fernando Santana, L., Simó, S., Dixon, R.E., Dickson, E.J., 2021. IP3R-driven increases in mitochondrial Ca2+ promote neuronal death in NPC disease. Proc. Natl. Acad. Sci. USA 118. https://doi.org/10.1073/PNAS.2110629118.
Vanier, M.T., 2010. Niemann-pick disease type C. Orphanet J. Rare Dis. 5, 16. https://doi.org/10.1186/1750-1172-5-16.
Weber, C.M., Moiz, B., Zic, S.M., Alpízar Vargas, V., Li, A., Clyne, A.M., 2024. Induced pluripotent stem cell-derived cells model brain microvascular endothelial cell glucose metabolism. Fluids Barriers CNS 19, 1–15. https://doi.org/10.1186/S12987-022-00395-Z/FIGURES/6.
Winkler, E.A., Nishida, Y., Sagare, A.P., Rege, S.V., Bell, R.D., Perlmutter, D., Sengillo, J. D., Hillman, S., Kong, P., Nelson, A.R., Sullivan, J.S., Zhao, Z., Meiselman, H.J., Wenby, R.B., Soto, J., Abel, E.D., Makshanoff, J., Zuniga, E., De Vivo, D.C., Zlokovic, B.V., 2015. GLUT1 reductions exacerbate Alzheimer's disease vasculo-neuronal dysfunction and degeneration. Nat. Neurosci. 18, 521–530. https://doi.org/10.1038/nn.3966.
Woo Suk, A., Antoniewicz, M.R., 2013. Parallel labeling experiments with [1,2-13C] glucose and [U-13C]glutamine provide new insights into CHO cell metabolism. Metab. Eng. 15, 34–47. https://doi.org/10.1016/j.ymben.2012.10.001.
Xue, X., Liu, B., Hu, J., Bian, X., Lou, S., 2022. The potential mechanisms of lactate in mediating exercise-enhanced cognitive function: a dual role as an energy supply substrate and a signaling molecule. Nutrition Metabol. 19 (1), 1–16. https://doi.org/10.1186/S12986-022-00687-Z.
Yazdani, S., Jaldin-Fincati, J.R., Pereira, R.V.S., Klip, A., 2019. Endothelial cell barriers: transport of molecules between blood and tissues. Traffic. https://doi.org/10.1111/tra.12645.
Yu, J., Vodyanik, M.A., Smuga-Otto, K., Antosiewicz-Bourget, J., Frane, J.L., Tian, S., Nie, J., Jonsdottir, G.A., Ruotti, V., Stewart, R., Slukvin, I.I., Thomson, J.A., 2007. Induced pluripotent stem cell lines derived from human somatic cells. Science 318, 1917–1920. https://doi.org/10.1126/SCIENCE.1151526.
Zilberter, Y., Zilberter, M., 2017. The vicious circle of hypometabolism in neurodegenerative diseases: ways and mechanisms of metabolic correction. J. Neurosci. Res. 95, 2217–2235. https://doi.org/10.1002/JNR.24064.